

1 **Long, S.P., Gordon, S.M., and Soignard, E., 2017, Distributed north-vergent shear and**
2 **flattening through Greater and Tethyan Himalayan rocks: Insights from metamorphic and**
3 **strain data from the Dang Chu region, central Bhutan: Lithosphere,**
4 **<https://doi.org/10.1130/L655.1>.**

5
6
7
8 **Table S1** (following two pages): Details on Dang Chu transect thin sections, listed from
9 structurally-low to high. Cells highlighted in gray represent paired thin sections from the same
10 sample used for strain analyses.

thin section number	original thin section number	latitude (dd,ddd)	longitude (dd,ddd)	height relative to base Pz (m)	map unit	lithology	foliation (d,d) ¹	lineation (tr,pl) ²	crenulation cleavage axis (tr,pl) ²	orientation relative to lineation	thin section orientation (d,d) ¹	major mineral phases ³	quartz recrystallization mechanism ⁴	kinematic indicators
78	BU13-78	27.48667	89.89397	-5620	GHml	granite	-	-	-	random	not oriented	qz,pl,ktfs	CBE	-
103A	BU13-103A	27.48494	89.90569	-5260	GHml	paragneiss	19, 140	20, 096	-	parallel to lineation	84, 264	qz,ms,grt,ktfs	CBE	-
103B	BU13-103B	27.48494	89.90569	-5260	GHml	paragneiss	-	-	-	parallel to lineation	not oriented	qz,ms,grt,ktfs	CBE	-
104A	BU13-104A	27.49025	89.92844	-4460	GHml	quartz vein	25, 358	25, 354	-	parallel to lineation	87, 265	qz,sil,grt	CBE	-
104C	BU13-104C	27.49025	89.92844	-4460	GHml	paragneiss	-	-	-	parallel to lineation	not oriented	qz,ms,grt,sil,ktfs	CBE	-
105	BU13-105	27.49036	89.93103	-4300	GHml	granite	-	-	-	random	not oriented	qz,ktfs,ms,sil	CBE	-
107A	BU13-107A	27.50575	89.96292	-3050	Ghlo	orthogneiss	21, 040	8, 330	-	parallel to lineation	71, 242	qz,pl,grt,sil	CBE	-
107B	BU13-107B	27.50575	89.96292	-3050	Ghlo	orthogneiss	-	-	-	parallel to lineation	not oriented	qz,ms,grt,pl	CBE	-
108	BU13-108	27.50481	89.98214	-2760	Ghlo	leucosome	34, 335	30, 306	-	parallel to lineation	88, 244	qz,pl,ms,sil	CBE	-
109	BU13-109	27.50333	90.00622	-2150	Ghlo	leucosome	-	-	-	parallel to lineation	not oriented	ktfs,qz,pl,grt	GBM	-
110	BU13-110	27.50217	90.01958	-1550	GHlm	granite	-	-	-	random	not oriented	pl,qz,ktfs,pl,ms	CBE	-
111A	BU13-111A	27.49856	90.03136	-1100	GHlm	paragneiss	07, 115	07, 120	-	parallel to lineation	89, 209	qz,pl,ktfs,ms	GBM	-
111B	BU13-111B	27.49856	90.03136	-1100	GHlm	leucosome	-	-	-	parallel to lineation	not oriented	ktfs,qz,pl,ms	CBE	-
112	BU13-112	27.49772	90.05614	-90	GHlm	leucosome	14, 046	8, 359	-	parallel to lineation	80, 271	qz,ktfs,tur,ms,pl	GBM	-
131A	BU13-131A	27.49942	90.05850	70	Cheka	leucosome	-	-	-	random	not oriented	ktfs,qz,ms,pl	GBM	-
131BA	BU13-131BA	27.49942	90.05850	70	Cheka	schist	10, 045	4, 348	-	parallel to lineation	82, 269	qz,ms,grt,sil	GBM	top-S SC fabric
131BB	BU13-131BB	27.49942	90.05850	70	Cheka	schist	10, 045	4, 348	-	normal to lineation	84, 170	qz,ms,pl,grt,sil	GBM	-
116A	BU13-116A	27.54264	90.11036	160	Cheka	quartzite	33, 290	26, 335	-	parallel to lineation	70, 055	qz,grt,ms	SGR	top-N SC fabric
116C	BU13-116C	27.54264	90.11036	160	Cheka	quartzite	48, 325	47, 332	-	parallel to lineation	47, 060	qz,ms,tur	GBM	top-N SC fabric
115	BU13-115	27.51869	90.10344	270	Cheka	granite	-	-	-	random	not oriented	qz,ktfs,pl,tur	GBM	-
130A	BU13-130A	27.50311	90.06475	710	Cheka	quartzite	16, 058	0, 148	-	parallel to lineation	72, 238	qz,grt,ms	GBM	-
130B	BU13-130B	27.50311	90.06475	710	Cheka	phyllite	51, 030	32, 330	-	parallel to lineation	56, 266	qz,ms,grt,pl,sil	GBM	top-S C-type shear bands
130C	BU13-130C	27.50311	90.06475	710	Cheka	pegmatite	-	-	-	random	not oriented	pl,qz,ktfs,ms,pl,tur	GBM	-
114A	BU13-114A	27.51236	90.09447	720	Cheka	phyllite	29, 270	0, 000	41, 270	parallel to lineation	61, 090	qz,ms,grt,grt	SGR	top-N asymmetric folds, rotated grt
114B	BU13-114B	27.51236	90.09447	720	Cheka	phyllite	29, 270	0, 000	41, 270	normal to lineation	90, 000	qz,ms,grt,grt	SGR	-
129A	BU13-129A	27.49969	90.07014	790	Cheka	phyllite	21, 060	2, 142	-	parallel to lineation	69, 230	qz,grt,ktfs	SGR	-
129B	BU13-129B	27.49969	90.07014	790	Cheka	phyllite	21, 060	2, 142	-	normal to lineation	85, 321	qz,grt,ktfs	SGR	-
128A	BU13-128A	27.50450	90.07872	910	Cheka	phyllite	26, 350	27, 000	-	parallel to lineation	86, 090	qz,ms,grt,grt	SGR	-
128C	BU13-128C	27.50450	90.07872	910	Cheka	quartzite	19, 040	11, 347	-	parallel to lineation	75, 232	qz,ms,grt,grt	SGR	-
117	BU13-117	27.54492	90.12442	910	Cheka	quartzite	42, 055	20, 350	-	parallel to lineation	56, 275	qz,ms,pl,chl	GBM	-
121A	BU13-121A	27.56708	90.17622	1210	Cheka	marble	horizontal	-	-	north-south	90, 000	cal,qz	not recrystallized	-
121B	BU13-121B	27.56708	90.17622	1210	Cheka	marble	horizontal	-	-	east-west	90, 000	cal,qz	not recrystallized	-
118A	BU13-118A	27.54747	90.13567	1240	Cheka	phyllite quartzite	21, 070	14, 340	-	parallel to lineation	69, 250	qz,ms,grt	not recrystallized	top-N rotated bt porphyroblasts
118BA	BU13-118BA	27.54747	90.13567	1240	Cheka	quartzite	12, 044	06, 338	-	parallel to lineation	79, 250	qz,cal	not recrystallized	-
118BB	BU13-118BB	27.54747	90.13567	1240	Cheka	quartzite	21, 070	14, 340	-	normal to lineation	85, 159	qz,cal	not recrystallized	-
118C	BU13-118C	27.54747	90.13567	1240	Cheka	granite	-	-	-	random	not oriented	qz,ktfs	SGR	-
113AA	BU13-113AA	27.50733	90.08442	1270	Cheka	phyllite	44, 310	4, 226	44, 315	parallel to lineation	46, 139	qz,ms,grt,grt	not recrystallized	-
113AB	BU13-113AB	27.50733	90.08442	1270	Cheka	phyllite	44, 310	4, 226	44, 315	normal to lineation	83, 046	qz,ms,grt,grt	not recrystallized	-
113B	BU13-113B	27.50733	90.08442	1270	Cheka	phyllite	-	-	-	parallel to lineation	not oriented	qz,ms,grt,grt	SGR	-
113C	BU13-113C	27.50733	90.08442	1270	Cheka	phyllite quartzite	-	-	-	parallel to lineation	not oriented	qz,ms,grt,grt	SGR	-
113D	BU13-113D	27.50733	90.08442	1270	Cheka	granite	-	-	-	random	not oriented	ktfs,pl,qz,ms	not recrystallized	-
113E	BU13-113E	27.50733	90.08442	1270	Cheka	phyllite quartzite	64, 000	54, 049	-	parallel to lineation	67, 103	qz,ms,grt	not recrystallized	-
119	BU13-119	27.54264	90.15417	1340	Cheka	quartzite	16, 345	-	16, 000	normal to crenulation	85, 088	qz,ms,grt	SGR	-
120AA	BU13-120AA	27.53983	90.16672	1450	Cheka	quartzite	10, 340	11, 352	-	parallel to lineation	87, 081	qz,cal,ms	SGR	-
120AB	BU13-120AB	27.53983	90.16672	1450	Cheka	quartzite	10, 340	11, 352	-	parallel to lineation	80, 170	qz,cal,ms	SGR	-
120B	BU13-120B	27.53983	90.16672	1450	Cheka	phyllite quartzite	12, 004	10, 352	-	parallel to lineation	88, 263	qz,cal,ms	not recrystallized	top-to-N SC fabric
81	BU14-81	27.54450	90.17144	1490	Cheka	marble	-	-	-	random	not oriented	cal,qz	SGR	-
122	BU13-122	27.56861	90.17947	1630	Cheka	slate	48, 025	-	31, 085	normal to crenulation	59, 264	qz,ms,hem,grt	not recrystallized	-
80A	BU14-80A	27.57706	90.18369	1960	Cheka	marble	47, 000	-	3, 087	normal to crenulation	86, 266	cal,qz	not recrystallized	-
123A	BU13-123A	27.58058	90.19064	2420	Deshchilling	phyllite quartzite	71, 350	33, 057	-	parallel to lineation	41, 010	bt,ms,hem,qz	not recrystallized	-
123BA	BU13-123BA	27.58058	90.19064	2420	Deshchilling	phyllite	82, 325	25, 052	-	parallel to lineation	19, 343	ms,pl,qz,hem	not recrystallized	-
123BB	BU13-123BB	27.58058	90.19064	2420	Deshchilling	phyllite	82, 325	25, 052	-	normal to lineation	65, 231	ms,pl,qz,hem	not recrystallized	-
79A	BU14-79A	27.58814	90.18742	2740	Deshchilling	phyllite quartzite	26, 315	-	13, 252	normal to crenulation	73, 073	qz,bt,gr,cal	not recrystallized	top-to-N SC fabric
124A	BU13-124A	27.59558	90.18669	3000	Deshchilling	phyllite	19, 000	-	5, 085	parallel to crenulation	88, 267	ms,qz,grt	GBAR	-
124B	BU13-124B	27.59558	90.18669	3000	Deshchilling	phyllite	19, 000	-	5, 085	parallel to crenulation	71, 174	ms,qz,grt	GBAR	-

78A	BU14-78A	27.60594	90.18894	3680	Deshchilling	phyllitic quartzite	39, 340	-	0, 250	normal to crenulation	90, 070	ms,qz,bt	not recrystallized	-
125AA	BU13-125AA	27.61111	90.19183	3980	Deshchilling	phyllite	16, 094	-	16, 100	normal to crenulation	74, 280	ms,qz,bt	GBAR	top-5 SC fabric, asymmetric boudinage
125AB	BU13-125AB	27.61111	90.19183	3980	Deshchilling	phyllite	16, 094	-	4, 100	parallel to crenulation	89, 188	ms,qz,bt	GBAR	-
125B	BU13-125B	27.61111	90.91830	3980	Deshchilling	quartzite	16, 070	15, 049	-	parallel to lineation	84, 320	qz,ms,bt	GBAR	-
77A	BU14-77A	27.61986	90.19564	4460	Deshchilling	quartzite	66, 230	9, 143	-	parallel to lineation	27, 073	qz,grt,dt,ms,tur	GBAR	-
126A	BU13-126A	27.62661	90.19764	4700	Deshchilling	phyllitic quartzite	28, 060	11, 353	-	parallel to lineation	65, 268	qz,ms,br,grt,p,tur	not recrystallized	top-to-N leucogranite o-object
126B	BU13-126B	27.62661	90.19764	4700	Deshchilling	granite	-	-	-	parallel to lineation	not oriented	pl,qz,dt,tur	not recrystallized	-
73	BU14-73	27.63939	90.19883	4830	Deshchilling	marble	-	-	-	random	not oriented	cal,qz,ms	not recrystallized	-
74A	BU14-74A	27.64314	90.20075	4930	Maneining	phyllite	28, 090	-	14, 154	parallel to crenulation	75, 332	gr,br,ms,qz,hem	not recrystallized	top-to-N rotated hem porphyroblasts
74B	BU14-74B	27.64314	90.20075	4930	Maneining	phyllite	28, 090	-	14, 154	normal to crenulation	65, 237	gr,br,ms,qz,hem	not recrystallized	-
75	BU14-75	27.65972	90.19569	5080	Maneining	phyllite	-	-	-	parallel to lineation	not oriented	gr,ms,qz,dt	GBAR	-
76	BU14-76	27.65047	90.19719	5250	Maneining	phyllite	-	-	-	normal to crenulation	not oriented	gr,ms,br,qz,cal	GBAR	-

¹(d, dd) stands for dip, dip direction notation. ²(tr, pl) stands for trend, plunge notation. ³Mineral abbreviations after Whitney and Evans (2010).

⁴GBR = subgrain rotation, GBM = grain boundary migration without chessboard extinction, CBE = grain boundary migration with chessboard extinction, GBAR = grain boundary area reduction

Discussion S1: Methodology and supporting data for RSCM thermometry

Measurements were made at the LeRoy Eyring Center for Solid State Science at Arizona State University, using a Raman spectrometer custom-built by E. Soignard. Carbonaceous material (CM) was analyzed *in situ* on polished, foliation-normal, lineation-parallel thin sections. The 532 nm laser was focused using a 50x ultra-long working distance Mitutoyo objective and attenuated to a power of 3 mW at the sample. The probed area of CM for each measurement was approximately 1 μm in diameter (see Fig. 8 in the text). Instrument parameters, settings, and procedures followed those outlined in Cooper et al. (2013), Long and Soignard (2016), and Long et al. (2016). The laser was focused on CM situated beneath a transparent grain (typically quartz or calcite), after procedures outlined in Beyssac et al. (2003). CM was analyzed for 120 seconds over a spectral window of 1100-2000 cm^{-1} . Multiple grains of CM were analyzed from each sample (the total range is between 10 and 15 grains per sample), to allow evaluation of in-sample variation.

The center positions, heights, widths, and areas of four first-order Raman peaks, including the G peak and three defect bands, D1, D2, and D3, are shown for individual analyses on Table S2. These parameters were determined using a peak fitting program written in Matlab by E. Soignard, which allowed peaks to be fit by a combination of Gaussian and Lorentzian peak shape, and background slope to be removed by using a 1st-order polynomial. R1 and R2 correspond to the height and area ratios as defined in equations 1 and 2 of Rahl et al. (2005), and the peak temperature (T_{peak}) for each analysis is calculated from equation 3 of Rahl et al. (2005). Analyses of each sample on Table S2 are ordered from low to high peak temperature. Standard means of R1, R2, and T_{peak} for all analyses from each sample are shown. The internal variation of R1, R2, and T_{peak} from each sample is represented by 1 standard deviation on the mean. However, the calibration equation of Rahl et al. (2005) also introduces an external ± 50 $^{\circ}\text{C}$ uncertainty in T_{peak} . Therefore, after Cooper et al. (2013), in order to present a more representative uncertainty, we calculated a propagated standard error (SE) by adding internal and external uncertainties quadratically, and dividing by the square root of the number of analyses (n). Mean T_{peak} with this propagated 2 SE uncertainty is reported for each sample on Table 1 in the text. At 2 SE, typical error ranges are ± 35 -60 $^{\circ}\text{C}$.

44 **Table S2** (following 5 pages): Supporting data for RSCM peak temperature determinations. Data
45 for individual CM spot analyses for each sample are shown, and are ordered from low to high
46 temperature.

sample and spot number	peak center position				peak width				peak amplitude				peak area				ratios		T _{peak} (°C)
	D1	D3	G	D2	D1	D3	G	D2	D1	D3	G	D2	D1	D3	G	D2	R1	R2	
BU13-103A_spot10	1350	1530	1582	1621	57	100	16	20	360	90	5400	420	32233	9571	135717	8933	0.067	0.182	564
BU13-103A_spot14	1349	1530	1582	1620	48	100	17	19	500	0	5500	400	31611	0	146869	8082	0.091	0.169	586
BU13-103A_spot15	1352	1540	1582	1620	55	70	17	19	200	50	3200	430	16163	3722	85451	8689	0.063	0.147	600
BU13-103A_spot19	1352	1530	1582	1620	50	75	17	15	320	0	7000	200	25133	0	186925	3190	0.046	0.117	627
BU13-103A_spot11	1352	1530	1582	1619	43	100	16	20	370	0	7600	240	23377	0	191009	5105	0.049	0.107	639
BU13-103A_spot17	1350	1540	1581	1618	45	70	16	19	310	0	6850	290	20497	0	172159	5860	0.045	0.103	642
BU13-103A_spot9	1351	1520	1581	1618	48	120	16	14	230	0	7800	50	17342	0	183373	744	0.029	0.086	655
BU13-103A_spot20	1345	1530	1582	1619	65	65	17	20	110	80	4400	320	11231	5530	117496	6806	0.025	0.083	657
BU13-103A_spot21	1351	1530	1582	1620	45	65	16	15	220	0	7600	130	15551	0	191009	2074	0.029	0.075	667
BU13-103A_spot7	1355	1550	1581	1610	55	70	16	50	150	0	8000	0	12959	0	201062	0	0.019	0.061	678
BU13-103A_spot18	1353	1530	1582	1622	49	75	16	15	140	20	7080	120	10080	1595	177940	1914	0.020	0.053	687
BU13-103A_spot13	1352	1530	1582	1621	30	100	16	13	200	0	6900	220	9425	0	173416	3042	0.029	0.051	692
BU13-103A_spot22	1353	1530	1582	1620	39	65	16	15	100	0	6500	0	6126	0	163363	0	0.015	0.036	704
BU13-103A_spot16	1351	1540	1582	1620	42	70	16	19	120	0	8700	0	7405	0	218655	0	0.014	0.033	707
BU13-103A_spot12	1355	1530	1581	1619	30	100	16	20	90	0	8100	0	4241	0	203575	0	0.011	0.020	719
mean:																	0.037	0.088	655
1σ (internal):																	0.022	0.048	44
1 SE (internal):																	0.006	0.012	11
prop. 2 SE (internal and external):																			35
n:																			15
BU13-113E_spot3	1349	1530	1581	1620	41	65	22	20	180	0	300	40	8972	0	10367	851	0.600	0.444	427
BU13-113E_spot26	1352	1540	1582	1623	41	75	19	12	2470	0	9900	490	123111	0	276381	6253	0.249	0.303	489
BU13-113E_spot24	1363	1540	1582	1625	53	70	16	18	330	120	3620	0	27473	8933	90981	0	0.091	0.232	518
BU13-113E_spot7	1353	1530	1580	1619	65	65	20	22	66	0	560	25	5215	0	17593	585	0.118	0.223	536
BU13-113E_spot16	1357	1550	1582	1623	41	70	18	9	1100	0	5950	550	47963	0	162799	5264	0.185	0.222	557
BU13-113E_spot20	1352	1530	1582	1621	37	55	19	20	450	20	3450	550	22775	1170	102966	11698	0.130	0.166	601
BU13-113E_spot9	1345	1530	1578	1615	75	65	18	20	11	0	230	7	1003	0	6083	149	0.048	0.139	604
BU13-113E_spot15	1353	1550	1581	1622	44	70	18	11	870	0	7900	230	40710	0	223367	2691	0.110	0.153	608
BU13-113E_spot12	1350	1530	1580	1618	50	65	20	24	41	0	430	23	2180	0	12636	587	0.095	0.142	616
BU13-113E_spot25	1361	1540	1582	1625	47	75	17	18	310	50	5300	0	19191	3988	127816	0	0.058	0.131	616
BU13-113E_spot19	1359	1520	1582	1621	42	75	18	19	270	70	4600	350	14936	5583	130062	7072	0.059	0.098	651
BU13-113E_spot22	1359	1510	1582	1625	38	70	18	18	220	30	3950	90	11011	2233	111684	1723	0.056	0.089	660
BU13-113E_spot21	1361	1520	1582	1621	40	65	18	17	180	60	4100	70	10214	4148	115925	1266	0.044	0.080	666
BU13-113E_spot18	1363	1530	1582	1622	47	70	17	13	170	0	6300	80	12551	0	168232	1106	0.027	0.069	672
BU13-113E_spot17	1362	1530	1581	1621	45	70	17	9	180	50	8000	100	12723	3722	213628	957	0.022	0.056	685
mean:																	0.126	0.170	594
1σ (internal):																	0.140	0.100	72
1 SE (internal):																	0.036	0.026	19
prop. 2 SE (internal and external):																			45
n:																			15
BU13-114_spot1	1351	1510	1581	1622	40	75	21	16	360	0	820	70	18967	0	24428	1191	0.439	0.425	409
BU13-114_spot18	1352	1530	1583	1621	43	70	22	18	1150	0	1850	400	60115	0	63931	7657	0.622	0.456	419
BU13-114_spot4	1355	1520	1581	1621	53	80	22	18	33	2	145	6	2747	170	5011	115	0.228	0.349	434
BU13-114_spot7	1352	1530	1583	1622	44	70	22	18	1750	6	3600	550	89700	447	120389	10528	0.486	0.407	440
BU13-114_spot17	1352	1530	1582	1623	46	70	21	14	1710	0	4600	350	95625	0	151739	5211	0.372	0.379	441
BU13-114_spot6	1356	1530	1582	1617	45	70	23	18	28	6	110	10	1660	447	3974	191	0.255	0.285	510
BU13-114_spot10	1356	1530	1582	1624	38	70	17	11	2800	0	15500	1450	134745	0	400537	16962	0.181	0.244	532
BU13-114_spot15	1356	1530	1582	1622	44	70	20	14	350	55	1800	150	18721	4094	56549	2233	0.194	0.242	538
BU13-114_spot12	1355	1530	1581	1621	43	70	20	18	450	50	2500	310	25487	3722	78540	5934	0.180	0.232	545
BU13-114_spot11	1356	1530	1582	1624	41	70	18	11	600	0	3900	250	32402	0	110270	2925	0.154	0.223	547
BU13-114_spot9	1357	1530	1583	1623	31	70	17	12	750	0	3050	900	28264	0	78815	11486	0.246	0.238	557
BU13-114_spot5	1357	1525	1583	1617	39	70	25	10	27	7	110	22	1387	521	4320	234	0.245	0.233	562
BU13-114_spot14	1357	1530	1582	1624	47	70	20	12	570	50	3980	100	32568	3722	125035	1276	0.143	0.205	563
BU13-114_spot16	1358	1530	1582	1623	49	70	19	12	350	55	3650	150	24329	4094	108935	1914	0.096	0.180	575
BU13-114_spot8	1357	1530	1583	1623	43	70	17	13	500	0	4300	230	25046	0	114825	3180	0.116	0.175	587
mean:																	0.264	0.285	511
1σ (internal):																	0.145	0.090	61
1 SE (internal):																	0.038	0.023	16
prop. 2 SE (internal and external):																			41
n:																			15
BU13-121_spot10	1351	1550	1582	1617	48	70	25	25	100	0	245	24	7540	0	9000	638	0.408	0.439	386
BU13-121_spot8	1353	1550	1581	1619	47	70	25	25	90	0	197	29	6644	0	7736	771	0.457	0.439	399
BU13-121_spot11	1353	1540	1582	1619	52	75	26	27	105	10	285	24	8577	798	11640	689	0.368	0.410	407
BU13-121_spot9	1350	1550	1581	1620	49	70	25	12	70	0	210	50	5388	0	8247	638	0.333	0.377	433
BU13-121_spot7	1352	1550	1581	1618	42	70	23	22	140	0	420	40	9236	0	15174	936	0.333	0.364	447
BU13-121_spot18	1354	1550	1583	1623	44	75	23	19	1130	0	4000	210	78100	0	144513	4243	0.282	0.344	454
BU13-121_spot17	1355	1550	1583	1623	44	75	23	19	1200	0	4300	240	82938	0	155352	4849	0.279	0.341	457
BU13-121_spot20	1353	1550	1582	1621	49	75	20	19	790	0	4850	300	54914	0	152367	6062	0.163	0.257	513
BU13-121_spot13	1348	1550	1581	1618	61	75	17	19	430	50	4950	550	41202	3988	132183	11113	0.087	0.223	527
BU13-121_spot19	1356	1550	1584	1617	46	75	27	23	1220	0	4050	470	65376	0	166219	11496	0.301	0.269	540
BU13-121_spot14	1355	1550	1582	1619	47	75	17	19	400	0	3950	320	29531	0	105479	6466	0.101	0.209	546
BU13-121_spot16	1355	1550	1582	1622	42	75	20	12	550	0	4700	100	36285	0	147655	1276	0.117	0.196	565
BU13-121_spot12	1357	1540	1582	1619	53	75	17	27	280	10	4850	24	23311	798	129512	689	0.058	0.153	599

BU13-121_spot15 BU13-121_spot21	1356	1550	1582	1619	47	75	17	19	330	0	5400	0	24363	0	144199	0	0.061	0.145	602		
	1354	1550	1582	1624	49	75	17	20	290	0	4600	40	20158	0	122836	851	0.063	0.140	608		
	mean:																	0.227	0.287	498	
																		1σ (internal):	0.135	0.104	74
																		1 SE (internal):	0.035	0.027	19
																		prop. 2 SE (internal and external):			46
																		n:			15
BU13-122_spot18	1347	1550	1582	1616	77	70	21	29	1400	70	5750	900	152925	5211	189674	27757	0.243	0.413	370		
BU13-122_spot16	1349	1550	1582	1613	71	70	20	30	2070	30	7600	1350	193579	2233	238761	43071	0.272	0.407	384		
BU13-122_spot11	1349	1550	1581	1614	73	70	21	30	2130	70	10000	1150	220578	5211	329867	36690	0.213	0.376	401		
BU13-122_spot19	1347	1550	1581	1617	70	70	21	25	1460	0	6550	930	144981	0	216063	24726	0.223	0.376	404		
BU13-122_spot20	1349	1550	1581	1615	71	70	20	29	1750	0	9300	950	176261	0	292168	29299	0.188	0.354	417		
BU13-122_spot22	1349	1550	1582	1617	68	70	19	23	950	0	5300	770	85087	0	158179	18834	0.179	0.325	445		
BU13-122_spot13	1348	1540	1581	1616	71	70	20	24	1200	0	8100	700	120865	0	254469	17866	0.148	0.307	455		
BU13-122_spot14	1349	1540	1581	1615	62	70	18	30	1170	0	7600	750	102905	0	207945	23928	0.154	0.307	457		
BU13-122_spot9	1351	1550	1581	1615	55	75	18	25	950	0	7650	640	76773	0	216299	17016	0.124	0.248	511		
BU13-122_spot15	1350	1540	1583	1619	55	70	20	20	320	0	2000	700	24967	0	60803	14889	0.160	0.248	522		
BU13-122_spot21	1351	1550	1582	1619	55	70	19	21	400	0	4100	600	33441	0	122365	13400	0.098	0.198	557		
BU13-122_spot23	1347	1550	1581	1617	66	70	18	20	450	0	5000	470	36105	0	141372	9997	0.090	0.193	560		
mean:																	0.174	0.313	457		
																	1σ (internal):	0.054	0.073	63	
																	1 SE (internal):	0.016	0.021	18	
																	prop. 2 SE (internal and external):			47	
																	n:			12	
BU13-124_spot16	1355	1540	1583	1623	47	75	25	16	1400	0	4200	370	96682	0	154280	6296	0.333	0.376	434		
BU13-124_spot10	1354	1550	1583	1620	43	70	24	17	1130	0	3200	170	64000	0	112845	3073	0.353	0.356	461		
BU13-124_spot13	1353	1540	1584	1621	44	75	25	15	1300	0	4100	560	84046	0	155807	8933	0.317	0.338	470		
BU13-124_spot15	1351	1540	1583	1621	42	75	25	17	1200	0	3650	650	74054	0	134077	11751	0.329	0.337	475		
BU13-124_spot8	1355	1550	1583	1622	47	70	26	16	1000	0	3200	280	66674	0	130690	4764	0.313	0.330	478		
BU13-124_spot7	1354	1550	1583	1621	45	70	26	18	1000	0	3400	410	61554	0	134374	7848	0.294	0.302	502		
BU13-124_spot17	1352	1540	1583	1621	52	75	25	15	750	0	4300	360	59282	0	157953	5743	0.174	0.266	507		
BU13-124_spot11	1356	1550	1582	1616	57	70	24	22	670	0	6200	650	59989	0	211088	15208	0.108	0.210	547		
BU13-124_spot14	1352	1540	1583	1620	61	75	25	16	400	0	3800	430	38327	0	144406	7317	0.105	0.202	555		
BU13-124_spot4	1355	1550	1582	1617	66	70	22	21	590	0	5100	400	47338	0	176243	8933	0.116	0.204	556		
BU13-124_spot9	1356	1550	1583	1621	45	70	22	17	650	0	5150	120	41494	0	172223	2169	0.126	0.192	572		
BU13-124_spot18	1355	1540	1583	1622	42	75	23	17	750	0	6000	200	43088	0	195767	3616	0.125	0.178	586		
BU13-124_spot5	1359	1550	1582	1619	50	70	22	16	590	0	5100	200	35862	0	176243	3403	0.116	0.166	596		
mean:																	0.216	0.266	518		
																	1σ (internal):	0.101	0.073	51	
																	1 SE (internal):	0.028	0.020	14	
																	prop. 2 SE (internal and external):			40	
																	n:			13	
BU13-125A_spot2	1361	1540	1583	1614	62	75	23	22	46	0	212	12	4480	0	5928	281	0.217	0.430	344		
BU13-125A_spot6	1354	1540	1584	1625	53	75	24	18	60	0	190	10	4995	0	6353	191	0.316	0.433	369		
BU13-125A_spot3	1354	1540	1582	1613	55	75	24	22	60	0	275	31	5016	0	7689	725	0.218	0.395	382		
BU13-125A_spot4	1355	1540	1583	1617	43	75	24	24	60	0	220	20	3922	0	5615	510	0.273	0.390	403		
BU13-125A_spot1	1352	1540	1583	1622	51	75	23	22	45	0	205	10	3372	0	6928	234	0.220	0.320	463		
BU13-125A_spot11	1356	1540	1582	1621	40	75	19	11	700	0	3300	190	36880	0	95308	2223	0.212	0.274	509		
BU13-125A_spot15	1354	1540	1582	1617	45	75	21	20	900	0	5200	210	59508	0	165991	4467	0.173	0.259	514		
BU13-125A_spot13	1356	1540	1582	1612	40	75	19	30	380	0	1900	320	21563	0	51211	10209	0.200	0.260	521		
BU13-125A_spot17	1355	1540	1581	1619	48	75	21	16	1000	0	5700	370	60787	0	181952	6296	0.175	0.244	531		
BU13-125A_spot16	1355	1540	1581	1622	43	75	21	11	750	0	6700	240	47386	0	213873	2808	0.112	0.181	579		
BU13-125A_spot18	1359	1540	1581	1619	51	75	20	16	250	0	2500	0	16147	0	76003	0	0.100	0.175	582		
BU13-125A_spot7	1356	1540	1581	1623	39	75	22	9	250	0	1350	170	10369	0	45146	1627	0.185	0.181	601		
BU13-125A_spot14	1357	1540	1582	1615	36	75	22	25	380	0	2600	340	18712	0	86948	9040	0.146	0.163	609		
BU13-125A_spot9	1360	1540	1582	1617	39	75	20	22	270	0	2650	420	15472	0	83252	9826	0.102	0.143	617		
BU13-125A_spot10	1356	1540	1581	1610	44	75	19	25	470	0	6850	450	30386	0	198497	11964	0.069	0.126	625		
mean:																	0.181	0.265	510		
																	1σ (internal):	0.065	0.103	93	
																	1 SE (internal):	0.017	0.027	24	
																	prop. 2 SE (internal and external):			55	
																	n:			15	
BU13-129_spot12	1351	1530	1582	1623	46	70	20	20	1800	30	3650	430	121661	2233	114668	9146	0.493	0.496	347		
BU13-129_spot6	1350	1540	1581	1620	44	75	19	18	250	0	500	50	13930	0	14923	957	0.500	0.467	379		
BU13-129_spot5	1350	1540	1581	1617	42	75	20	25	190	0	400	40	10106	0	12566	1063	0.475	0.446	396		
BU13-129_spot15	1351	1520	1582	1621	40	80	18	20	3000	0	8400	700	164144	0	237504	14889	0.357	0.394	421		
BU13-129_spot10	1354	1530	1582	1623	38	75	18	10	1870	80	4350	1850	97201	6381	122993	19674	0.430	0.405	428		
BU13-129_spot3	1350	1540	1581	1622	42	75	20	12	200	0	870	30	11064	0	26449	383	0.230	0.292	495		
BU13-129_spot17	1353	1520	1581	1622	41	80	18	12	1300	0	8400	210	72023	0	237504	2680	0.155	0.226	544		
BU13-129_spot11	1354	1530	1582	1623	65	75	18	30	270	0	4000	70	25787	0	113097	2233	0.068	0.183	563		
BU13-129_spot4	1350	1540	1581	1615	42	75	18	12	50	0	450	10	2766	0	12723	128	0.111	0.177	583		
BU13-129_spot8	1356	1540	1582	1623	40	75	18	10	800	0	9100	140	40525	0	248986	1489	0.088	0.139	617		
BU13-129_spot14	1366	1520	1581	1611	50	80	15	17	140	0	4700	270	10996	0	110741	4881	0.030	0.087	654		
BU13-129_spot13	1360	1520	1583	1618	60	70	15	20	180	60	7700	120	16965	4467	181427	2552	0.023	0.084	655		
BU13-129_spot7	1353	1540	1582	1620	42	75	19	18	390	0	7500	50	19082	0	216609	957	0.052	0.081	667		

																mean:	0.232	0.267	519
																1σ (internal):	0.184	0.150	110
																1 SE (internal):	0.051	0.042	31
																prop. 2 SE (internal and external):			67
																n:			13
BU13-130A_spot16	1351	1540	1582	1619	70	80	19	23	800	150	3850	980	79442	12762	114904	23971	0.208	0.364	412
BU13-130A_spot13	1350	1540	1581	1612	52	100	18	28	2350	0	10700	1000	173353	0	302535	29777	0.220	0.343	438
BU13-130A_spot12	1350	1540	1577	1612	59	100	23	24	800	0	3650	450	62169	0	131868	11486	0.219	0.302	481
BU13-130A_spot17	1349	1540	1582	1620	60	80	18	17	650	0	8500	250	59282	0	240332	4520	0.076	0.195	553
BU13-130A_spot6	1339	1520	1580	1618	55	80	18	16	57	0	680	30	4129	0	19227	510	0.084	0.173	579
BU13-130A_spot4	1344	1520	1580	1616	60	80	15	14	45	0	730	40	3419	0	17200	596	0.062	0.161	585
BU13-130A_spot2	1350	1520	1580	1620	55	80	18	15	33	0	470	15	2299	0	13289	239	0.070	0.145	605
BU13-130A_spot18	1350	1550	1582	1608	35	70	21	24	300	0	3100	550	16493	0	89048	14038	0.097	0.138	620
BU13-130A_spot3	1350	1520	1580	1618	50	80	16	15	31	0	610	15	1963	0	15331	239	0.051	0.112	634
BU13-130A_spot15	1355	1540	1581	1612	55	100	15	28	125	0	10000	0	9753	0	235619	0	0.013	0.040	699
																mean:	0.110	0.197	561
																1σ (internal):	0.072	0.100	86
																1 SE (internal):	0.023	0.032	27
																prop. 2 SE (internal and external):			63
																n:			10
BU13-131B_spot20	1350	1550	1583	1623	41	70	16	16	470	0	2530	100	27336	0	63586	1702	0.186	0.295	479
BU13-131B_spot7	1352	1540	1582	1622	38	80	19	13	1700	0	4500	230	68700	0	128664	3180	0.378	0.343	481
BU13-131B_spot13	1351	1520	1582	1622	51	70	22	13	700	20	3000	200	47022	1489	103673	2765	0.233	0.306	481
BU13-131B_spot5	1355	1540	1581	1615	65	80	20	18	15	0	115	6	1185	0	3613	115	0.130	0.241	521
BU13-131B_spot14	1356	1520	1582	1620	45	70	18	14	300	20	2400	380	17096	1489	65667	5658	0.125	0.193	570
BU13-131B_spot19	1350	1550	1583	1622	41	70	16	18	250	0	2670	40	15061	0	67104	766	0.094	0.182	573
BU13-131B_spot15	1358	1520	1583	1620	40	70	19	14	220	0	2100	450	11591	0	62675	6700	0.105	0.143	618
BU13-131B_spot18	1351	1550	1583	1610	40	70	15	50	135	0	3150	0	8482	0	74220	0	0.043	0.103	641
BU13-131B_spot3	1354	1540	1581	1624	50	80	16	10	5	0	100	0	266	0	2270	0	0.050	0.105	641
BU13-131B_spot16	1357	1530	1581	1618	60	80	18	14	130	30	3950	50	10274	2552	111684	744	0.033	0.084	658
BU13-131B_spot23	1355	1550	1583	1623	35	70	14	16	95	0	2770	0	4886	0	58948	0	0.034	0.077	666
BU13-131B_spot17	1358	1530	1582	1620	60	80	15	14	90	30	4350	100	7113	2552	102494	1489	0.021	0.064	676
BU13-131B_spot22	1353	1550	1584	1623	39	70	14	16	45	0	3100	0	2490	0	68173	0	0.015	0.035	704
BU13-131B_spot24	1355	1550	1583	1623	39	70	15	16	40	0	2900	0	2292	0	66123	0	0.014	0.034	705
BU13-131B_spot21	1350	1550	1583	1623	41	70	15	16	10	0	2870	0	582	0	67623	0	0.003	0.009	729
																mean:	0.098	0.148	610
																1σ (internal):	0.100	0.104	84
																1 SE (internal):	0.026	0.027	22
																prop. 2 SE (internal and external):			50
																n:			15
BU14-74A_spot10	1355	1530	1585	1621	38	80	23	16	3600	0	5000	1600	201005	0	168973	27225	0.720	0.506	387
BU14-74A_spot11	1355	1530	1584	1621	40	80	23	16	2800	0	4500	1200	158883	0	152076	20419	0.622	0.479	395
BU14-74A_spot8	1354	1530	1584	1621	40	80	23	17	3300	0	6700	1500	187255	0	218606	27119	0.493	0.432	415
BU14-74A_spot6	1353	1530	1584	1623	41	80	27	19	1750	0	2850	550	101784	0	109161	11113	0.614	0.458	415
BU14-74A_spot3	1354	1530	1585	1622	36	80	23	20	2900	0	4500	850	142805	0	146825	18079	0.644	0.464	415
BU14-74A_spot7	1353	1530	1585	1622	38	80	26	17	2650	0	4500	750	142853	0	165976	13559	0.589	0.443	426
BU14-74A_spot5	1353	1530	1584	1623	41	80	26	15	3290	0	6150	1050	177668	0	218722	16750	0.535	0.430	427
BU14-74A_spot1	1354	1530	1585	1622	39	80	25	18	1500	0	2300	420	77052	0	84487	8040	0.652	0.454	428
BU14-74A_spot4	1354	1530	1585	1623	38	80	27	20	2400	0	3450	640	124749	0	132143	13612	0.696	0.461	430
BU14-74A_spot12	1354	1530	1584	1623	40	80	23	18	1900	0	4400	550	107814	0	148696	10528	0.432	0.404	430
BU14-74A_spot2	1354	1530	1585	1622	36	80	25	20	1900	0	2850	510	93562	0	101075	10847	0.667	0.455	430
BU14-74A_spot9	1354	1530	1584	1620	40	80	26	19	1600	0	2900	450	90790	0	110788	9093	0.552	0.431	430
BU14-74A_spot14	1355	1530	1585	1621	41	80	25	18	2000	0	3800	700	112165	0	139586	13400	0.526	0.423	432
BU14-74A_spot13	1351	1530	1584	1621	39	80	27	20	2800	0	4500	590	143831	0	172360	12549	0.622	0.438	438
BU14-74A_spot15	1354	1530	1585	1622	38	80	25	19	2250	0	4400	740	123893	0	167207	14952	0.511	0.405	448
																mean:	0.592	0.446	423
																1σ (internal):	0.079	0.026	15
																1 SE (internal):	0.020	0.007	4
																prop. 2 SE (internal and external):			27
																n:			15
BU14-75_spot3	1351	1530	1582	1623	46	70	21	14	940	0	2450	200	56953	0	80817	2978	0.384	0.413	408
BU14-75_spot7	1354	1530	1582	1623	42	70	18	12	750	0	2200	150	39892	0	62204	1914	0.341	0.384	428
BU14-75_spot8	1350	1530	1582	1622	42	70	20	16	2700	0	7150	500	143610	0	217369	8508	0.378	0.389	432
BU14-75_spot5	1352	1530	1582	1623	42	70	20	13	1150	0	4150	250	63618	0	126165	3456	0.277	0.329	469
BU14-75_spot1	1353	1530	1583	1622	45	70	19	16	776	0	3300	150	42451	0	98489	2552	0.235	0.296	492
BU14-75_spot13	1354	1530	1582	1623	45	75	20	12	1000	0	4600	300	54705	0	135179	3829	0.217	0.282	502
BU14-75_spot12	1352	1530	1582	1618	43	75	20	17	650	0	3350	120	36814	0	95046	2169	0.194	0.275	503
BU14-75_spot11	1353	1530	1582	1622	45	75	20	13	1000	0	4200	230	52422	0	127685	3180	0.238	0.286	504
BU14-75_spot10	1353	1530	1582	1623	40	75	20	12	1180	0	4900	150	59774	0	148966	1914	0.241	0.284	507
BU14-75_spot9	1354	1530	1581	1623	44	75	20	16	770	50	4000	300	46343	3988	121605	5105	0.193	0.268	510
BU14-75_spot2	1353	1530	1583	1623	46	70	19	12	776	0	4100	170	45205	0	122365	2169	0.189	0.266	511
BU14-75_spot4	1354	1530	1582	1623	42	70	19	10	870	0	4800	100	49982	0	143257	1063	0.181	0.257	519
BU14-75_spot15	1352	1530	1581	1622	44	75	21	14	1670	0	8500	450	89327	0	253220	6700	0.196	0.256	524
BU14-75_spot6	1352	1530	1582	1622	42	70	19	10	1020	0	5900	210	58599	0	176086	2233	0.173	0.247	527
																mean:	0.246	0.302	488

																1 σ (internal):	0.070	0.053	37
																1 SE (internal):	0.019	0.014	10
																prop. 2 SE (internal and external):			33
																n:			14
BU14-76_spot14	1353	1520	1583	1621	44	80	26	20	3150	0	6300	690	182555	0	228212	14676	0.500	0.429	420
BU14-76_spot8	1351	1520	1583	1622	41	80	25	20	5100	0	9200	1100	264805	0	314609	23396	0.554	0.439	422
BU14-76_spot7	1352	1520	1583	1621	41	80	25	18	4300	0	8300	750	232211	0	294359	14357	0.518	0.429	424
BU14-76_spot11	1352	1520	1583	1622	41	80	26	17	2000	0	4600	400	116325	0	175732	7232	0.435	0.389	447
BU14-76_spot10	1353	1520	1584	1623	41	80	27	18	2120	0	5400	420	123305	0	214229	8040	0.393	0.365	462
BU14-76_spot1	1354	1530	1584	1622	46	75	25	17	1280	0	3500	300	71579	0	128567	5424	0.366	0.348	473
BU14-76_spot9	1352	1520	1583	1624	41	80	26	20	2170	0	5000	480	121699	0	204204	10209	0.434	0.362	475
BU14-76_spot13	1352	1520	1583	1621	42	80	26	18	2150	0	6250	480	123518	0	230522	9188	0.344	0.340	475
BU14-76_spot15	1354	1520	1583	1622	46	80	26	20	1230	0	4200	230	80264	0	160451	4892	0.293	0.327	475
BU14-76_spot12	1353	1520	1583	1622	44	80	25	16	1050	0	3600	200	63195	0	132240	3403	0.292	0.318	485
BU14-76_spot6	1356	1520	1584	1623	44	80	25	20	680	0	2000	100	39409	0	78540	2127	0.340	0.328	487
BU14-76_spot2	1354	1530	1584	1623	45	75	26	15	1450	0	3950	390	76012	0	145690	6221	0.367	0.333	489
BU14-76_spot4	1355	1530	1583	1622	45	75	26	17	1450	0	4400	350	79322	0	162288	6328	0.330	0.320	493
BU14-76_spot3	1353	1530	1583	1621	44	75	26	17	1450	0	4950	350	80796	0	176044	6328	0.293	0.307	497
BU14-76_spot5	1359	1520	1584	1623	52	80	30	25	1150	390	3550	500	75731	33180	167290	13293	0.324	0.312	500
																mean:	0.386	0.356	468
																1 σ (internal):	0.082	0.043	27
																1 SE (internal):	0.021	0.011	7
																prop. 2 SE (internal and external):			29
																n:			15
BU14-77AA_spot16	1349	1500	1583	1623	44	100	22	18	640	0	1300	55	35662	0	42023	1053	0.492	0.453	392
BU14-77AA_spot1	1351	1530	1582	1623	46	75	24	21	1190	50	2370	250	77654	3988	89347	5583	0.502	0.450	398
BU14-77AA_spot2	1349	1530	1582	1622	42	75	24	18	1700	0	3150	300	97666	0	118752	5743	0.540	0.440	418
BU14-77AA_spot4	1351	1530	1582	1624	45	75	22	15	480	0	1500	60	30642	0	51836	957	0.320	0.367	440
BU14-77AA_spot8	1354	1530	1582	1622	50	75	28	14	1110	0	2750	180	73101	0	120951	2680	0.404	0.377	452
BU14-77AA_spot5	1352	1530	1582	1620	50	75	24	18	1750	0	5400	90	110810	0	203575	1723	0.324	0.352	457
BU14-77AA_spot19	1350	1500	1583	1623	44	100	24	16	190	0	640	25	11435	0	21790	425	0.297	0.340	463
BU14-77AA_spot7	1354	1530	1582	1619	49	75	27	14	1170	0	3300	200	72603	0	139958	2978	0.355	0.337	481
BU14-77AA_spot6	1347	1530	1574	1613	50	75	22	17	5650	0	25000	1700	357759	0	836035	30734	0.226	0.292	494
BU14-77AA_spot20	1349	1500	1583	1619	44	100	24	17	168	0	720	35	10111	0	24513	633	0.233	0.287	501
BU14-77AA_spot21	1349	1500	1583	1618	42	100	24	18	205	0	950	39	11777	0	31187	747	0.216	0.269	516
BU14-77AA_spot15	1355	1530	1582	1620	44	75	20	18	480	0	2700	90	25675	0	82083	1723	0.178	0.235	541
BU14-77AA_spot18	1347	1500	1583	1622	43	100	22	18	170	0	850	23	8145	0	26528	440	0.200	0.232	551
BU14-77AA_spot22	1351	1500	1583	1622	44	100	21	16	157	0	1150	20	9449	0	35484	340	0.137	0.209	557
BU14-77AA_spot11	1353	1530	1581	1622	45	75	22	12	620	0	4300	100	36748	0	138999	1276	0.144	0.208	560
																mean:	0.305	0.323	481
																1 σ (internal):	0.127	0.082	54
																1 SE (internal):	0.033	0.021	14
																prop. 2 SE (internal and external):			38
																n:			15
BU14-78A_spot19	1338	1480	1607	1622	105	200	42	16	6500	1150	10800	20	968194	244599	712513	340	0.602	0.576	287
BU14-78A_spot25	1336	1490	1603	1650	110	180	50	50	4250	1100	7600	0	615760	210568	481233	0	0.559	0.561	293
BU14-78A_spot23	1340	1500	1603	1650	110	170	53	50	3000	900	5400	0	434654	162711	362444	0	0.556	0.545	309
BU14-78A_spot11	1352	1540	1578	1612	53	80	20	28	880	230	6700	580	73262	19568	210487	17271	0.149	0.359	400
BU14-78A_spot3	1345	1530	1575	1613	52	80	22	25	950	70	4300	300	67573	5955	148597	7976	0.221	0.301	483
BU14-78A_spot18	1347	1530	1577	1614	49	80	21	18	1470	0	8850	340	98527	0	291932	6508	0.166	0.248	524
BU14-78A_spot17	1347	1530	1576	1610	60	80	16	28	390	80	5050	150	32008	6806	126920	4467	0.077	0.196	552
BU14-78A_spot16	1355	1520	1577	1613	70	100	18	30	380	450	5300	480	35036	47856	149854	15314	0.072	0.175	573
BU14-78A_spot12	1343	1540	1569	1606	53	80	19	26	920	100	10800	400	64223	8508	322327	11060	0.085	0.162	591
BU14-78A_spot5	1344	1530	1564	1613	69	80	17	25	190	0	4190	0	17933	0	111888	0	0.045	0.138	604
BU14-78A_spot13	1348	1520	1575	1615	40	80	18	17	500	300	5890	240	26343	25523	166536	4339	0.085	0.134	621
BU14-78A_spot15	1350	1520	1575	1614	40	80	18	17	270	0	5000	290	14773	0	141372	5243	0.054	0.092	656
BU14-78A_spot6	1360	1530	1575	1613	69	80	16	25	120	0	6700	0	11326	0	168389	0	0.018	0.063	676
																mean:	0.207	0.273	505
																1 σ (internal):	0.207	0.175	134
																1 SE (internal):	0.057	0.049	37
																prop. 2 SE (internal and external):			79
																n:			13
BU14-80A_spot5	1351	1530	1583	1621	43	80	23	18	1900	0	3700	530	107610	0	129357	10146	0.514	0.435	417
BU14-80A_spot13	1353	1530	1583	1622	43	80	23	19	2050	0	4700	370	116105	0	164319	7476	0.436	0.403	432
BU14-80A_spot9	1353	1530	1583	1622	45	80	25	14	1550	0	4400	320	95409	0	161626	4764	0.352	0.364	452
BU14-80A_spot10	1352	1530	1583	1622	44	80	23	18	1590	0	4600	300	95696	0	166190	5743	0.346	0.358	457
BU14-80A_spot14	1353	1520	1583	1622	43	70	26	20	1750	100	3950	350	102932	7444	161321	7444	0.443	0.379	459
BU14-80A_spot6	1352	1530	1583	1622	43	80	23	16	1750	0	4400	350	87662	0	148696	5955	0.398	0.362	466
BU14-80A_spot15	1352	1520	1583	1623	43	70	23	16	1550	0	4520	280	87787	0	163300	4764	0.343	0.343	472

BU14-80A_spot4	1353	1530	1583	1623	46	80	22	12	2350	0	9300	550	125930	0	311005	7019	0.253	0.284	510
BU14-80A_spot3	1354	1530	1583	1622	40	80	23	18	1440	0	5300	300	75867	0	185296	5743	0.272	0.284	516
mean:																	0.353	0.345	472
1 σ (internal):																	0.081	0.042	26
1 SE (internal):																	0.021	0.011	7
prop. 2 SE (internal and external):																			29
n:																			15
BU14-81_spot9	1363	1540	1582	1621	64	70	22	14	410	110	1930	150	34562	8189	66696	2233	0.212	0.334	445
BU14-81_spot10	1365	1540	1582	1622	64	70	22	14	360	50	1920	140	30347	3722	66350	2084	0.188	0.307	467
BU14-81_spot15	1360	1530	1581	1621	63	80	22	17	115	30	760	30	10645	2552	25415	542	0.151	0.291	473
BU14-81_spot14	1360	1530	1581	1621	65	70	21	20	155	50	1110	60	14804	3722	35433	1276	0.140	0.287	474
BU14-81_spot4	1352	1530	1581	1620	45	75	22	25	920	150	2400	270	44028	11964	82938	7178	0.383	0.328	498
BU14-81_spot11	1363	1540	1581	1622	75	80	23	7	110	10	785	15	10029	851	28361	112	0.140	0.260	503
BU14-81_spot5	1353	1530	1582	1620	47	75	22	20	700	50	2850	100	39996	3988	98489	2127	0.246	0.284	508
BU14-81_spot3	1352	1520	1581	1621	45	70	20	20	730	0	2750	150	34935	0	86394	3190	0.265	0.281	517
BU14-81_spot13	1357	1540	1580	1621	60	80	19	10	160	0	1570	60	14106	0	45344	638	0.102	0.235	518
BU14-81_spot2	1351	1520	1582	1619	45	70	21	18	940	50	3850	150	44985	3722	126999	2871	0.244	0.257	537
BU14-81_spot8	1365	1540	1582	1619	58	80	21	21	180	60	1370	60	12692	5105	45192	1340	0.131	0.214	550
BU14-81_spot6	1362	1530	1582	1620	65	75	20	20	135	5	1830	0	10667	399	57491	0	0.074	0.157	593
BU14-81_spot12	1357	1540	1580	1620	50	80	20	11	190	0	2450	90	13477	0	76969	1053	0.078	0.147	605
BU14-81_spot7	1355	1530	1582	1621	55	75	19	12	250	5	4670	80	16715	399	139377	1021	0.054	0.106	641
BU14-81_spot1	1352	1520	1574	1617	70	70	18	16	950	200	28500	1000	87589	14889	805819	17016	0.033	0.096	645
mean:																	0.163	0.239	532
1 σ (internal):																	0.091	0.075	61
1 SE (internal):																	0.024	0.019	16
prop. 2 SE (internal and external):																			41
n:																			15

Discussion S2: Methodology, sample descriptions, and supporting data for thermobarometry

Major-element phase compositions were collected using a five-spectrometer JEOL 8500F field emission electron microprobe at Washington State University using synthetic and natural standards for calibration and a ZAF correction routine. Quantitative wavelength dispersive spectroscopy (WDS) analyses on garnet, plagioclase, K-feldspar, biotite, and muscovite were made from core to rim within individual crystals to obtain quantitative spot analyses for thermobarometric calculations and also to check for zoning (Tables S3-S5; see Figure 9 in the text for quantitative element profiles). Operating conditions for WDS analyses were 15 kV accelerating voltage, 20 nA beam current, and 2 μm beam size (except for plagioclase where the beam was spread out to 5 μm). Representative compositions of garnet, biotite and muscovite, and feldspar are shown in Tables S3, S4, and S5, respectively.

Peak temperatures for all five samples were calculated using garnet-biotite exchange thermometry, specifically the 5AV model calibration of Holdaway (2000). Petrographic inspection and assessment of the zoning across the minerals was used to determine which compositions of the garnet and biotite were used for the analyses. The garnet composition with the lowest Mn and Fe# was combined with matrix biotite for the calculations; biotite did not show any zoning. Two-sigma errors are estimated at ± 25 $^{\circ}\text{C}$ (Holdaway, 2000).

Peak pressures for samples BU13-104C, BU13-131B, and BU13-130B were calculated using the program *THERMOCALC* using the internally-consistent dataset of Holland and Powell (2011) (version 3.33; Powell and Holland, 1994). Below, individual samples are described.

Greater Himalayan quartzite sample BU13-103A contains quartz, biotite, muscovite, and garnet. The garnet are subhedral and contain inclusions of quartz, ilmenite, zircon, and monazite. Pyrope and almandine show a concave down, bell pattern, with X_{Mg} and X_{Fe} varying from 0.09 and 0.82 in the core to 0.07 and 0.80 in the rim, respectively. Grossular and spessartine show the opposite pattern: X_{Ca} varies from 0.06 to 0.09 from core to rim. Spessartine is more weakly zoned, with X_{Mn} varying from 0.03 to 0.04. Biotite is unzoned, but shows compositional differences based on textural location. Matrix biotite reveals Fe# of 0.72–0.75 and Ti of 0.18–0.23 (atoms per formula unit (apfu) normalized on the basis of 11 O atoms), whereas biotite adjacent to garnet is variable (Fe# = 0.59–0.77 and Ti = 0.09–0.23 apfu). Muscovite shows a similar trend: matrix muscovite has Fe# = 0.66–0.70 and Ti = 0.04–0.05 versus muscovite adjacent to garnet is more variable (Fe# = 0.59–0.74 and Ti = 0.05–0.06).

Greater Himalayan metapelite sample BU13-104C consists of biotite, muscovite, and sillimanite layers that alternate with quartz-, plagioclase-, and K-feldspar-rich layers to define a strong foliation. Garnet is subhedral, resorbed, and contains quartz, biotite, ilmenite, monazite, and zircon inclusions. Garnet reveals a flat profile in the core, but retrogression effects toward the rim. Almandine decreases slightly from core ($X_{Fe} = 0.76$) to mantle ($X_{Fe} = 0.75$) and continues to decrease at the rim ($X_{Fe} = 0.72$). Pyrope shows a similar pattern with homogeneous $X_{Mg} = 0.15$ from core to mantle and a decrease to $X_{Mg} = 0.10$ at the rim. Spessartine shows the opposite pattern, with a homogeneous $X_{Mn} = 0.06$ between the core and mantle, and an increase in $X_{Mn} = 0.14$ at the rim. Grossular is homogeneous across the entire crystal, from $X_{Ca} = 0.03$ –0.04. Biotite inclusions have lower Fe# (0.46–0.50) in comparison to matrix biotite (0.62–0.59). Titanium ranges from 0.10–0.17 apfu. Muscovite is also unzoned; Fe# ranges from 0.51–0.55 and X_{Na} from 0.07–0.08. Both plagioclase and K-feldspar are found in the sample, and both are unzoned. Plagioclase ranges from An₁₉₋₂₃, whereas the K-feldspar has Or₈₄₋₉₀.

Deshichilling Formation siliceous gneiss sample BU13-126A is fine-grained and mainly consists of quartz and biotite, with lesser muscovite, plagioclase, and tourmaline. Garnet shows signs of late retrogression affecting ~100 μm closest to the rim; the garnet rims are skeletal. Almandine increases from core ($X_{Fe} = 0.33$) to rim ($X_{Fe} = 0.38$) before decreasing at the near rim

to $X_{\text{Fe}} = 0.36$. Both spessartine and pyrope decrease from core to rim, from $X_{\text{Mn}} = 0.44$ to 0.38 and $X_{\text{Mg}} = 0.02$ to 0.01, respectively. Spessartine increases at the near rim to $X_{\text{Mn}} = 0.45$ –0.43, whereas pyrope remains constant. The grossular zonation is more complicated. The X_{Ca} is relatively constant in the core of the grains, from 0.22–0.19, but increases to $X_{\text{Ca}} = 0.26$ before decreasing to 0.18–0.16. The X_{Ca} then increases to 0.20 at the rim likely due to late retrogression. Biotite is unzoned, with $\text{Fe}\# = 0.27$ –0.29 and $\text{Ti} = 0.07$ –0.13 apfu. Muscovite is minor in comparison to biotite and has variable composition, from $\text{Fe}\# = 0.55$ –0.71 and $X_{\text{Na}} = 0.02$ –0.03. Plagioclase is also variable (An_{16-30}) but does not show zoning.

Chekha Formation fine-grained metapelite sample BU13-130B consists of biotite, muscovite, and sillimanite that define a strong schistosity. Quartz, plagioclase, and garnet are also present. Quartz and biotite reveal inclusion trails that are sub-parallel to the main foliation. The garnet shows signs of late retrogression affecting $\sim 150 \mu\text{m}$ of the garnet closest to the rim. Almandine and spessartine decrease slightly from core to rim, X_{Fe} from 0.77 to 0.76 and X_{Mn} from 0.10 to 0.09, respectively, before increasing in the near rim back to their core values. Grossular shows the opposite pattern: $X_{\text{Ca}} = 0.04$ in the core to $X_{\text{Ca}} = 0.05$ toward the rim to $X_{\text{Ca}} = 0.04$ in the near rim. Pyrope is flat across the crystals at 0.10 before decreasing slightly to 0.09 at the near rim. Biotite is unzoned but heterogeneous across the sample. Biotite included within and adjacent to garnet have more variable $\text{Fe}\#$ (0.53–0.65) and Ti (0.10–0.16 apfu) in comparison to matrix garnet ($\text{Fe}\# = 0.60$ and $\text{Ti} = 0.12$ –0.15). Muscovite shows similar trends: matrix muscovite is unzoned and has $\text{Fe}\# = 0.49$ –0.52 and $X_{\text{Na}} = 0.13$ –0.15, whereas muscovite included in garnet has higher $\text{Fe}\#$ (0.54–0.55). Muscovite adjacent to garnet has $\text{Fe}\#$ from 0.49 to 0.57. Plagioclase is unzoned (An_{21-23}).

Chekha Formation garnet-sillimanite schist BU13-131B is very similar to sample BU13-130B, with a strong schistosity defined by mica and sillimanite, with quartz and plagioclase defining the other main matrix phases. Garnet is minor in the sample and is anhedral with skeletal rims affecting $\sim 250 \mu\text{m}$ closest to the rim. Spessartine is homogeneous across the entire grain ($X_{\text{Mn}} = 0.12$). Almandine is homogenous in the core ($X_{\text{Fe}} = 0.73$). It decreases slightly to $X_{\text{Fe}} = 0.72$ toward the rim before increasing to $X_{\text{Fe}} = 0.74$ in the rim. Grossular shows the opposite pattern: $X_{\text{Ca}} = 0.04$ in the core to $X_{\text{Ca}} = 0.05$ toward the near rim to $X_{\text{Ca}} = 0.04$ in the rim. Pyrope is flat across the crystals at 0.11 before decreasing slightly to 0.10 at the rim. Biotite and muscovite are unzoned and homogeneous across the samples. Biotite has $\text{Fe}\# = 0.54$ –0.61

and Ti of 0.13–0.16 apfu. For muscovite, Fe# is from 0.45 to 0.52, and X_{Na} shows a narrow range of 0.15 to 0.19. Plagioclase is also unzoned (An_{23-26}).

Table S3: Representative microprobe composition of garnet from Dang Chu samples.

Table S3: Representative microprobe composition of garnet from Dang Chu samples										
Sample	BU13-103A		BU13-103A		BU13-104C		BU13-104C		BU13-126A	
position	core	rim	core	rim	core	near rim	rim	core	rim	core
SiO ₂	37.00	37.09	37.34	37.28	37.29	37.58	37.10	37.16		
TiO ₂	bdl	bdl	0.06	0.02	0.15	0.12	0.11	0.03		
Al ₂ O ₃	21.00	21.12	20.49	20.93	20.73	20.91	21.19	20.98		
FeO	36.60	35.84	34.28	32.39	14.86	15.95	16.02	34.38		
MnO	1.42	1.80	2.59	6.30	19.11	16.95	18.86	4.27		
MgO	2.24	1.86	3.84	2.55	0.43	0.31	0.17	2.44		
CaO	2.15	2.92	1.24	1.13	7.34	8.53	7.05	1.29		
Cr ₂ O ₃	0.03	0.02	0.02	0.01	0.02	0.01	0.01	0.02		
Na ₂ O	bdl	bdl	0.01	bdl	bdl	bdl	bdl	bdl		
K ₂ O	0.01	0.01	0.01	bdl	0.01	0.01	0.02	0.01		
Total	100.45	100.66	99.89	100.61	99.94	100.38	100.53	100.57		
Cations per 12 oxygen										
Si	2.99	2.99	3.01	3.00	3.01	3.01	2.99	3.00		
Al	2.00	2.01	1.95	1.99	1.97	1.98	2.01	1.99		
Ti	0.00	0.00	0.00	0.00	0.01	0.01	0.01	0.00		
Fe	2.47	2.41	2.31	2.18	1.00	1.07	1.08	2.32		
Cr	0.00	0.00	0.00	0.00	0.00	0.00	0.00	0.00		
Mn	0.10	0.12	0.18	0.43	1.31	1.15	1.29	0.29		
Mg	0.27	0.22	0.46	0.31	0.05	0.04	0.02	0.29		
Ca	0.19	0.25	0.11	0.10	0.64	0.73	0.61	0.11		
Na	0.00	0.00	0.00	0.00	0.00	0.00	0.00	0.00		
K	0.00	0.00	0.00	0.00	0.00	0.00	0.00	0.00		
Total	8.01	8.01	8.02	8.00	7.99	7.99	8.00	8.01		
X _{Fe}	0.82	0.80	0.76	0.72	0.33	0.36	0.36	0.77		
X _{Mn}	0.03	0.04	0.06	0.14	0.44	0.38	0.43	0.10		
X _{Mg}	0.09	0.07	0.15	0.10	0.02	0.01	0.01	0.10		
X _{Ca}	0.06	0.08	0.04	0.03	0.21	0.24	0.20	0.04		
Fe#	0.90	0.92	0.83	0.88	0.95	0.97	0.98	0.89		
bdl = below detection limit										

BU13-130B	BU13-130B	BU13-131B	BU13-131B	BU13-131B
near rim	rim	core	near rim	rim
36.91	37.09	37.25	37.25	37.25
0.02	0.02	0.02	0.03	bdl
21.21	21.07	21.12	20.97	21.08
34.10	34.25	32.77	31.98	32.85
4.19	4.18	5.42	5.40	5.43
2.47	2.28	2.70	2.71	2.50
1.60	1.49	1.47	1.83	1.46
0.01	bdl	bdl	0.01	0.02
bdl	0.01	bdl	bdl	bdl
0.01	0.01	0.01	bdl	bdl
100.52	100.40	100.75	100.17	100.59
2.98	2.99	2.99	3.00	3.00
2.02	2.01	2.00	1.99	2.00
0.00	0.00	0.00	0.00	0.00
2.30	2.31	2.20	2.15	2.21
0.00	0.00	0.00	0.00	0.00
0.29	0.29	0.37	0.37	0.37
0.30	0.27	0.32	0.33	0.30
0.14	0.13	0.13	0.16	0.13
0.00	0.00	0.00	0.00	0.00
0.00	0.00	0.00	0.00	0.00
8.01	8.00	8.01	8.00	8.00
0.76	0.77	0.73	0.72	0.74
0.09	0.10	0.12	0.12	0.12
0.10	0.09	0.11	0.11	0.10
0.05	0.04	0.04	0.05	0.04
0.89	0.89	0.87	0.87	0.88

Table S4 (following page): Representative microprobe composition of biotite and muscovite from Dang Chu samples.

Table S4: Representative microprobe composition of biotite and muscovite from Dang Chu samples

Sample	BU13-126A	BU13-103A	BU13-104C	BU13-130B	BU13-131B	BU13-126A	BU13-103A	BU13-104C	BU13-130B	BU13-131B
	biotite matrix	biotite matrix	biotite matrix	biotite matrix	biotite matrix	muscovite matrix	muscovite matrix	muscovite matrix	muscovite matrix	muscovite matrix
SiO ₂	37.66	34.20	34.42	35.23	35.13	45.12	45.08	45.17	45.51	46.88
TiO ₂	1.26	3.14	2.51	1.90	2.77	0.44	1.47	0.66	0.85	0.78
Al ₂ O ₃	20.27	17.51	20.59	18.41	18.72	28.91	35.01	36.07	36.73	36.26
FeO	18.67	24.34	19.58	21.11	20.60	5.95	2.31	1.41	1.21	1.17
MnO	0.90	0.05	0.16	0.09	0.15	0.22	bdl	bdl	bdl	bdl
MgO	4.18	5.37	7.56	8.04	8.22	2.41	0.59	0.71	0.63	0.69
CaO	0.03	0.01	bdl	0.01	bdl	0.02	bdl	bdl	bdl	0.02
Na ₂ O	0.05	0.15	0.17	0.16	0.24	0.15	0.37	0.47	0.98	0.91
K ₂ O	9.10	9.23	9.46	8.46	8.31	9.84	9.82	10.14	8.85	6.84
Cr ₂ O ₃	bdl	0.07	0.02	0.02	0.02	bdl	bdl	0.02	0.02	0.01
F	1.63	0.33	0.20	0.28	0.25	1.77	0.08	bdl	bdl	0.07
Cl	bdl	0.07	0.01	0.01	0.01	bdl	bdl	bdl	bdl	0.01
Total	93.76	94.48	94.68	93.72	94.42	94.82	94.73	94.63	94.78	93.65
Cations per 11 oxygen										
Si	2.93	2.72	2.65	2.75	2.71	3.16	3.03	3.03	3.02	3.10
Ti	0.07	0.19	0.15	0.11	0.16	0.02	0.07	0.03	0.04	0.04
Al	1.86	1.64	1.87	1.69	1.70	2.38	2.77	2.85	2.87	2.83
Fe	1.21	1.62	1.26	1.38	1.33	0.35	0.13	0.08	0.07	0.07
Mn	0.06	0.00	0.01	0.01	0.01	0.01	0.00	0.00	0.00	0.00
Mg	0.48	0.64	0.87	0.93	0.94	0.25	0.06	0.07	0.06	0.07
Ca	0.00	0.00	0.00	0.00	0.00	0.00	0.00	0.00	0.00	0.00
Na	0.01	0.02	0.03	0.03	0.04	0.02	0.05	0.06	0.13	0.12
K	0.90	0.94	0.93	0.84	0.82	0.88	0.84	0.87	0.75	0.58
Total	7.52	7.77	7.77	7.74	7.71	7.07	6.95	6.99	6.94	6.81
Fe#	0.72	0.72	0.59	0.60	0.59	X _{Na}	0.06	0.06	0.15	0.17
Al (VI)	0.79	0.36	0.52	0.44	0.41					

bdl = below detection limit

Table S5: Representative microprobe composition of plagioclase and K-feldspar from Dang Chu samples.

Sample	BU13-126A	BU13-104C	BU13-104C	BU13-130B	BU13-131B
phase	plagioclase matrix	plagioclase matrix	k'feldspar matrix	plagioclase matrix	plagioclase matrix
SiO ₂	62.89	62.99	64.05	62.92	61.65
Al ₂ O ₃	23.74	23.62	19.23	23.19	24.25
FeO	0.03	0.01	0.07	0.04	0.03
CaO	4.48	4.38	0.01	4.58	5.05
Na ₂ O	9.16	9.14	1.65	8.91	8.73
K ₂ O	0.12	0.21	14.30	0.11	0.10
Total	100.42	100.35	99.31	99.75	99.81
Cations per 8 oxygen					
Si	2.77	2.78	2.96	2.79	2.74
Al	1.23	1.23	1.05	1.21	1.27
Fe	0.00	0.00	0.00	0.00	0.00
Ca	0.21	0.21	0.00	0.22	0.24
Na	0.78	0.78	0.15	0.77	0.75
K	0.01	0.01	0.84	0.01	0.01
Total	5.00	5.01	5.00	5.00	5.01
X _{Ab}	0.78	0.78	0.15	0.77	0.75
X _{An}	0.21	0.21	0.00	0.22	0.24
X _{Or}	0.01	0.01	0.85	0.01	0.01

Discussion S3: Methodology and supporting data for finite strain analyses

Two foliation-normal thin sections were analyzed from each finite strain sample (Tables 3, S1), following methods outlined in Long et al. (2011c). For the eight samples that exhibited mineral stretching lineation, one thin section was cut parallel to lineation, which approximates the XZ strain plane (thin sections ending with 'A'), and one was cut normal to lineation, which approximates the YZ strain plane (thin sections ending with 'B'). For the three samples that exhibited crenulation cleavage but not stretching lineation, the 'A' thin section was cut normal to crenulation cleavage, and the 'B' thin section was cut parallel to crenulation cleavage. For the one sample (121) that did not exhibit stretching lineation or crenulation cleavage, the 'A' thin

section was cut in a north-south orientation, which approximates lineation-parallel, and the ‘B’ thin section was cut in an east-west orientation, which approximates lineation-normal. Two types of quartz porphyroclast scenarios were analyzed. The most common was observed in phyllite and schist, where quartz porphyroclasts were isolated within a micaceous matrix ($n = 9$) (Figs. 11A, S1A-D). The second scenario was observed in marble and calcareous quartzite, where quartz porphyroclasts were isolated within a matrix of calcite ($n = 3$) (Fig. 11B).

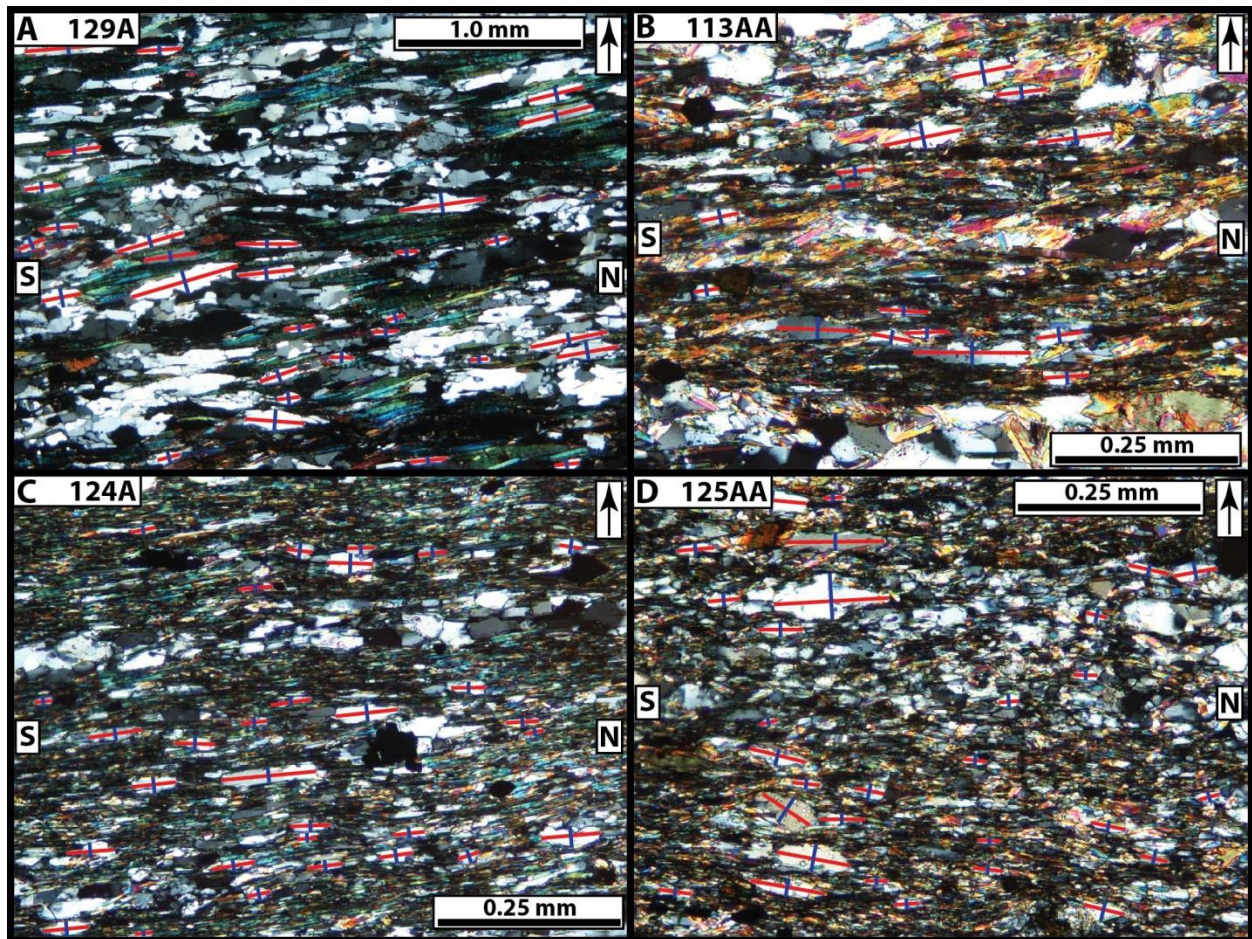
For each thin section, the Rf- ϕ method (e.g., Ramsay, 1967; Dunnet, 1969; Ramsay and Huber, 1983) was used to quantify a 2D strain ellipse. The final elongation (Rf; the ratio of the long axis to the short axis), and ϕ (defined here as the angle of inclination of the long axis measured relative to foliation), were measured for 30 quartz porphyroclasts on photomicrographs of each thin section. Photomicrographs were taken with the apparent dip of tectonic foliation oriented horizontal, north or east toward the right-hand side of the page, and structurally-upward toward the top of the page. Representative photomicrographs with measured grains annotated are shown in Figures 11 and S1, and Rf- ϕ plots showing data from individual grains measured on each thin section are shown in Figure S2.

The tectonic ellipticity (R_s) of each thin section was estimated using the harmonic mean of all Rf values (e.g., Lisle, 1977; 1979), and the mean of all ϕ values is reported as the overall ϕ value for the thin section. All analyses were equivalent to ‘situation B’ of Figure 5.5 of Ramsay and Huber (1983). Uncertainties reported for R_s and ϕ represent 1 standard error of all measurements (note: R_s values and uncertainties are rounded to the nearest single decimal place, and ϕ values and uncertainties are rounded to the nearest degree). Uncertainties in R_s range between ± 0.1 - 0.3 , and uncertainties in ϕ range between ± 1 - 4° . ϕ was measured relative to the apparent dip of foliation, which was oriented horizontal in each photomicrograph. Therefore, ϕ is equivalent to the parameter θ' , as defined by Ramsay and Huber (1983). The sign convention used for ϕ is: down to the north or east relative to foliation (clockwise from foliation in the photomicrographs) is positive, and down to the south or west relative to foliation (counterclockwise from foliation in the photomicrographs) is negative.

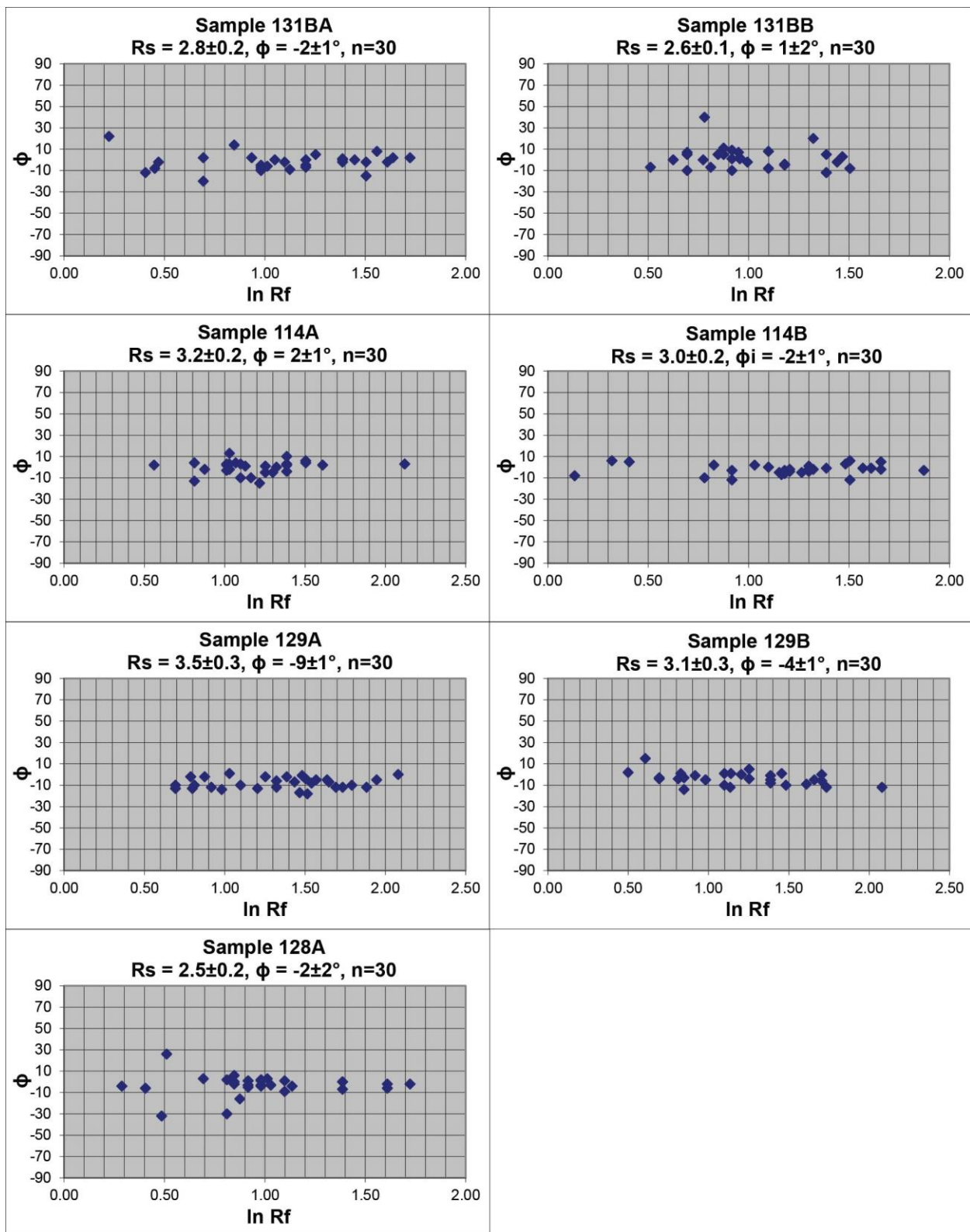
The R_s and ϕ values for the 2D strain ellipses from each ‘A’ and ‘B’ thin section were combined to generate the 3D strain ellipsoid for the sample (e.g., Long et al., 2011c). For all analyses, the Z axis was sub-normal to foliation in both the ‘A’ and ‘B’ thin sections, and was assigned an R_s value of 1.0 in both ellipses. The R_s values of both 2D ellipses were then directly

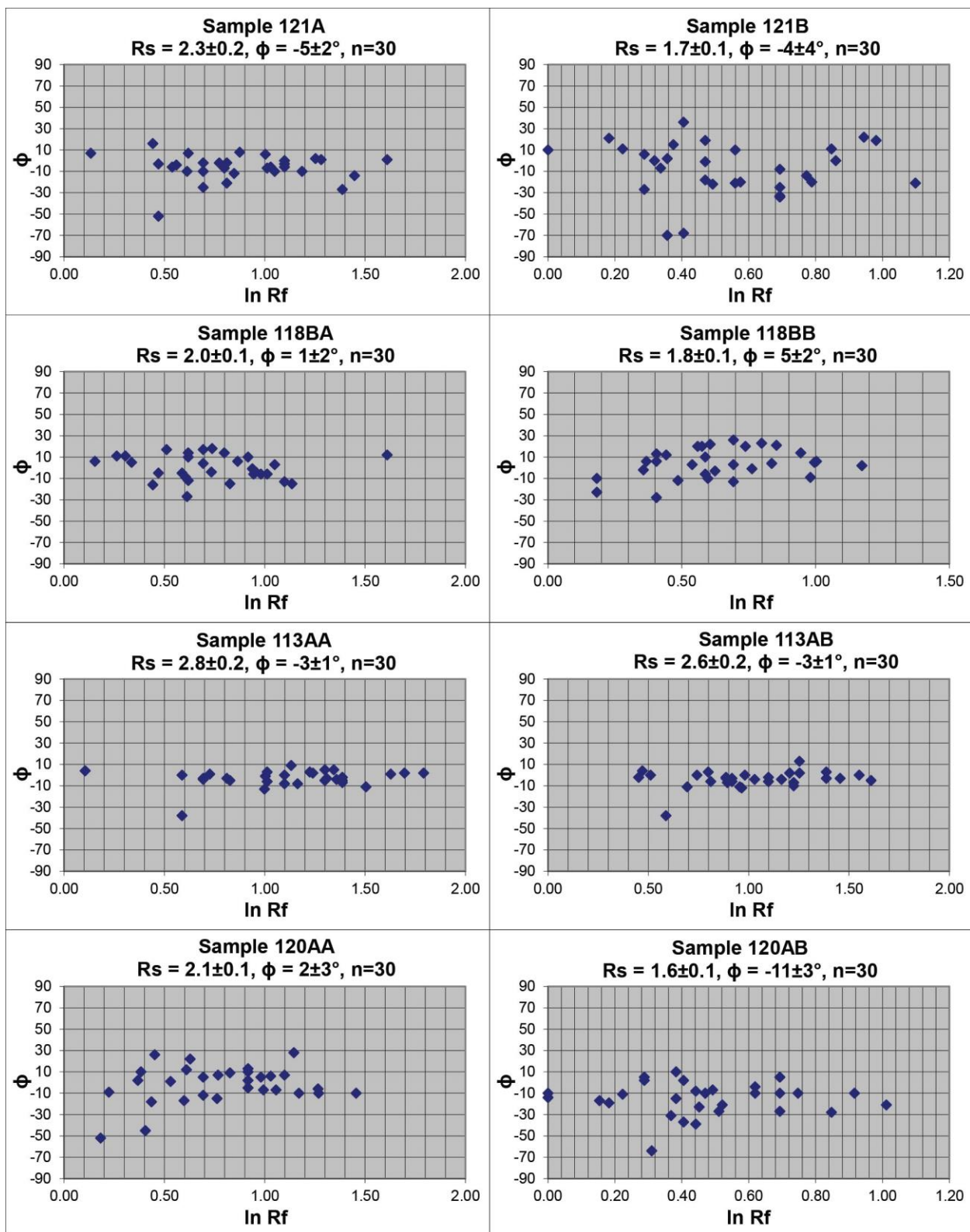
compared to assign the X and Y strain directions ($X > Y$), and the relative magnitudes of the axes of the 3D strain ellipsoid. In all analyses, R_s in the 'A' thin section was either greater than or equivalent within error to R_s in the 'B' thin section, and the shortening direction is approximately normal to foliation. This justified using foliation, lineation, and crenulation cleavage to approximate the principal strain directions within the studied rocks.

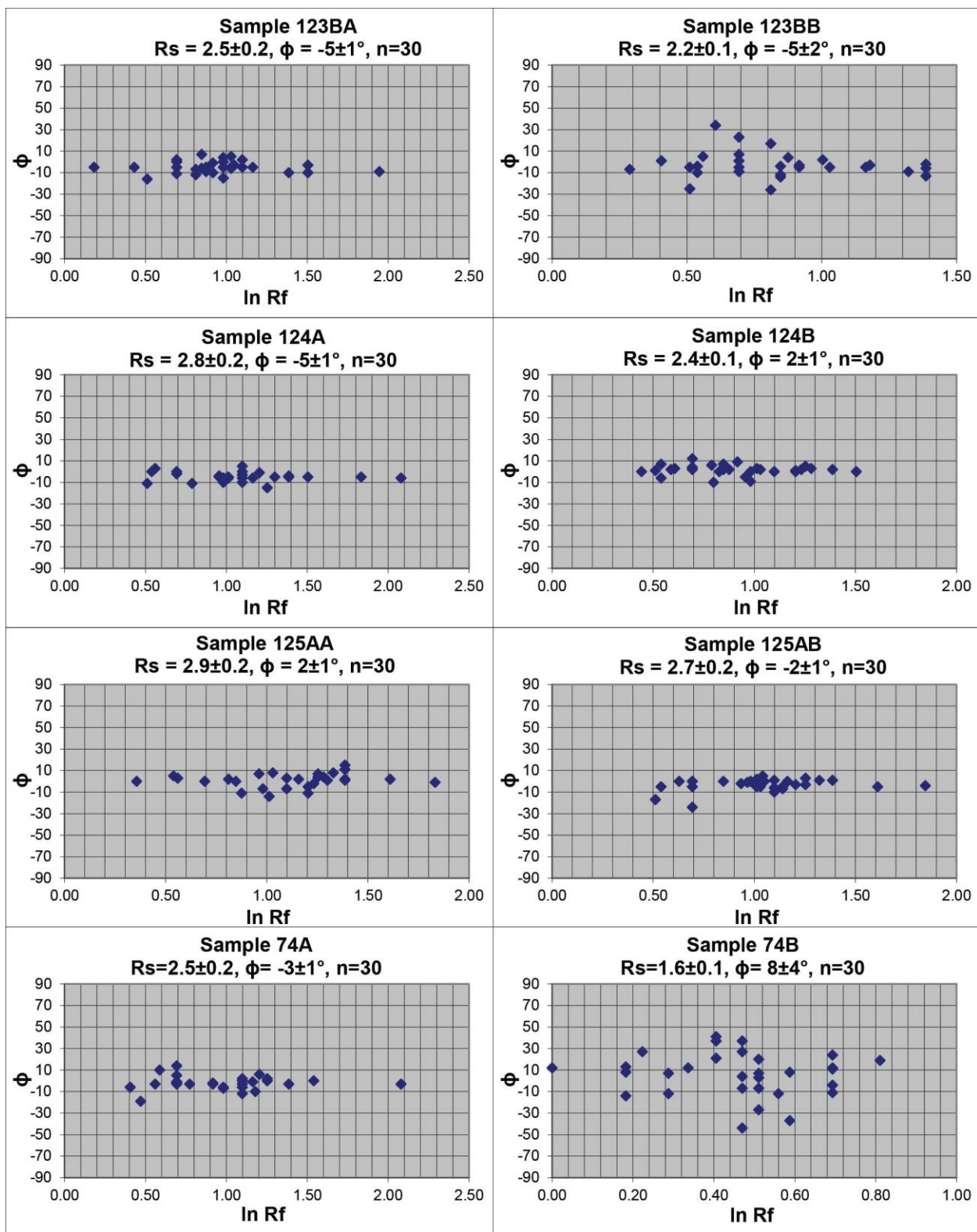
Figure S1: Annotated photomicrographs showing representative examples of quartz grain measurements for R_f - ϕ analyses, organized from structurally-low to high. All photos are taken in cross-polarized light, with tectonic foliation oriented horizontal. The arrow points structurally-upward. All photos are from lineation-parallel thin sections, and illustrate the scenario of non-recrystallized quartz porphyroclasts isolated within a micaceous matrix. The long axes of measured quartz porphyroclasts are shown in red, and short axes are shown in blue.



205 **Figure S2** (following three pages): R_f - ϕ graphs, plotting the natural log of final ellipticity (R_f)
206 versus the orientation of the long axis (ϕ) for individual quartz porphyroclasts. ϕ is measured
207 relative to foliation; a positive ϕ value is down to the north or east relative to foliation (i.e.,
208 clockwise relative to foliation in the photomicrographs), and a negative ϕ value is down to the
209 south or west relative to foliation (i.e., counterclockwise relative to foliation in the
210 photomicrographs). Errors reported for R_s and ϕ represent 1 standard error of all measurements.







213

214

215

Discussion S4: Methodology for estimation of mean kinematic vorticity with the R_s - θ' method

Assuming plane strain and idealized steady-state flow, the relationship between tectonic strain (R_s) and the angle between foliation and the long axis of the strain ellipsoid (θ') can be used to estimate mean kinematic vorticity (W_m) (Fossen and Tikoff, 1993; Tikoff and Fossen, 1995). W_m can be measured by plotting the R_s value of the lineation-parallel thin section ($R_s[x/z]$) versus the corresponding θ' value, and comparing to graphed lines of constant W_m (e.g., Tikoff and Fossen, 1995; Yonkee, 2005). This involves assumption that the orientation of tectonic foliation approximates a 'shear zone boundary', or boundary of a 'high strain zone' (Tikoff and Fossen, 1995). As illustrated in mapping in Bhutan and adjacent regions of the Himalaya, 1st-order Himalayan shear zones, such as the MCT, are oriented subparallel to macroscopic foliation for significant across-strike map distances, including ≥ 50 km in the Kuru Chu half window in eastern Bhutan (Long et al., 2011b), ≥ 60 km in the Darjeeling-Sikkim Himalaya (Bhattacharyya et al., 2015), and ≥ 110 km in the Arun half window in eastern Nepal (Schelling and Arita, 1991). This justifies the assumption that tectonic foliation is approximately parallel to the 'shear zone boundary' of major Himalayan structures such as the MCT. Accordingly, here we also apply this assumption to transport-parallel lengthening in the hanging wall and footwall of the MCT (e.g., Long et al., 2016).

Discussion S5: Compilation of published temperature and pressure data, estimation of structural height of samples, and estimation of N-S distance of samples along the MCT.

Table S6 shows a compilation of published temperature and pressure data from central Bhutan, which are plotted in Figure 12 in the text, and also includes information on sample location (plotted on Figure 2 in the text), lithology, map unit, structural height above the MCT (rounded to the nearest 50 m), and north-south distance measured along the trace of the MCT (rounded to the nearest 100 m). Below, details are given on how structural height and north-south distance were estimated.

Figure 12 includes data collected from the Sarpang, Shemgang, and Dang Chu transects (Table S6). For the Sarpang transect, structural distance relative to the MCT was measured from the projected locations of samples on the Sarpang cross-section of Long et al. (2016; their Fig. 2B). For the Shemgang transect, structural distance was measured from projection of samples onto the Mangde Chu cross-section of Long et al. (2011b). For the Dang Chu transect, the heights of samples on the Dang Chu tectonostratigraphic column (Fig. 5 in the text) were used. For the samples of Cooper et al. (2013) that were located at a significant distance from the Dang Chu transect line, heights relative to the base of the Chekha Formation were calculated from 3-point problems that incorporated topography and average dip angle of foliation. The heights of all Dang Chu transect samples were converted to height above the MCT by adding 5.7 km, the minimum observed thickness of GH rocks on the Dang Chu transect, to their height relative to the base of the Chekha Formation. This is supported by the map patterns of GH rocks to the west of the Dang Chu transect on Long et al. (2011d), which are deformed into a dome, and exhumed the lowest GH unit (GH1ml), exposing rocks that are at equivalent structural levels to those exposed just above the MCT ~60 km to the south. Thus, we interpret that the MCT is in the shallow subsurface at the latitude of the Dang Chu transect.

For estimation of north-south distances, the trace of the MCT on the Mangde Chu cross-section of Long et al. (2011b) was used as a reference point. All samples were projected to their corresponding foliation-normal position on the MCT. Distances of Shemgang transect samples were measured on the MCT on the Mangde Chu cross-section. For Sarpang transect samples, the position of the MCT trace on the Mangde Chu section was projected directly west to the Sarpang transect cross-section (Long et al. 2016; their Fig. 2B), and distances were measured along the MCT relative to this point. Dang Chu transect samples were projected directly east to their respective positions on the Mangde Chu cross-section, and their corresponding distances along the MCT trace were measured. The data are listed on Table S6 in km north of the southernmost sample (sample 1A of Long et al. 2016).

Table S6 (following two pages): Compilation of published temperature and pressure data from central Bhutan.

transect	data source	published sample number	original sample number	map unit on Long et al. (2011d)	lithology	latitude (dd,ddd)	longitude (dd,ddd)	structural height relative to MCT (km)	N-S distance along (km)	data type ¹ (°C)	T error (°C)	T error level (kbar)	P error level (kbar)
Dang Chu	this study	75	BU1-75	Maneting	phyllite	27.65972	90.19569	11.05	89.1	RSCM	488	33	2SE
Dang Chu	this study	76	BU14-76	Maneting	phyllite	27.65047	90.19719	10.95	88.1	RSCM	468	29	2SE
Dang Chu	this study	74A	BU14-74A	Maneting	phyllite	27.64314	90.20075	10.65	87.2	RSCM	423	27	2SE
Dang Chu	this study	126A	BU13-126A	Deshichiling	siliceous gneiss	27.62661	90.19764	10.40	85.3	P-T	566	25	2σ
Dang Chu	this study	77AA	BU14-77AA	Deshichiling	quartzite	27.61986	90.19564	10.15	84.6	RSCM	481	38	2SE
Dang Chu	this study	125A	BU13-125A	Deshichiling	phyllite	27.61111	90.19183	9.70	83.7	RSCM	510	55	2SE
Dang Chu	this study	78A	BU14-78A	Deshichiling	phyllitic quartzite	27.60594	90.18894	9.40	83.1	RSCM	505	79	2SE
Dang Chu	this study	124	BU13-124	Deshichiling	phyllite	27.59558	90.18669	8.70	81.9	RSCM	518	40	2SE
Dang Chu	this study	80A	BU14-80A	Chekha	marble	27.57706	90.18369	7.65	79.8	RSCM	472	29	2SE
Dang Chu	this study	122	BU13-122	Chekha	slate	27.56861	90.17947	7.35	78.9	RSCM	457	47	2SE
Dang Chu	this study	81	BU14-81	Chekha	marble	27.54450	90.17144	7.20	76.2	RSCM	532	41	2SE
Dang Chu	this study	113E	BU13-113E	Chekha	phyllitic quartzite	27.50733	90.08442	6.95	72.1	RSCM	594	45	2SE
Dang Chu	this study	121	BU13-121	Chekha	limestone	27.56708	90.17622	6.90	78.7	RSCM	498	46	2SE
Dang Chu	this study	129	BU13-129	Chekha	phyllite	27.49969	90.07014	6.50	71.3	RSCM	519	67	2SE
Dang Chu	this study	114	BU13-114	Chekha	phyllite	27.51236	90.09447	6.40	72.7	RSCM	511	41	2SE
Dang Chu	this study	130A	BU13-130A	Chekha	quartzite	27.50311	90.06475	6.40	71.6	RSCM	561	63	2SE
Dang Chu	this study	130B	BU13-130B	Chekha	metapelite	27.50311	90.06475	6.40	71.6	P-T	625	25	2σ
Dang Chu	this study	131B	BU13-131B	Chekha	schist	27.49942	90.05850	5.75	71.2	RSCM	610	50	2SE
Dang Chu	this study	131B	BU13-131B	Chekha	schist	27.49942	90.05850	5.75	71.2	P-T	647	25	2σ
Dang Chu	this study	104C	BU13-104C	GHlm	metapelite	27.49025	89.92844	1.25	70.2	P-T	634	25	2σ
Dang Chu	this study	103A	BU13-103A	GHlm	quartzite	27.48494	89.90569	0.45	69.6	RSCM	655	35	2SE
Dang Chu	this study	103A	BU13-103A	GHlm	quartzite	27.48494	89.90569	0.45	69.6	P-T	646	25	2σ
Dang Chu	this study	FB64		Pzu	calc-silicate	27.61700	90.03600	8.80	84.3	RSCM	508	33	2SE
Dang Chu	Cooper et al. (2013)	FB77		Pzu	slate	27.57700	90.04800	8.25	79.9	RSCM	420	21	2SE
Dang Chu	Cooper et al. (2013)	FB28		Pzu	marble	27.55100	90.20200	8.20	77.1	RSCM	430	30	2SE
Dang Chu	Cooper et al. (2013)	FB52		Chekha	schist	27.49600	90.16500	7.40	70.9	RSCM	544	28	2SE
Dang Chu	Cooper et al. (2013)	FB20		Chekha	quartzite	27.51800	90.25000	7.20	73.4	RSCM	569	29	2SE
Dang Chu	Cooper et al. (2013)	FB58		Chekha	quartzite	27.44500	90.12700	7.20	65.3	RSCM	549	34	2SE
Dang Chu	Cooper et al. (2013)	FB125		Chekha	paragneiss	27.52000	90.29900	6.65	73.6	RSCM	556	31	2SE
Dang Chu	Cooper et al. (2013)	FB125		Chekha	paragneiss	27.52000	90.29900	6.65	73.6	P-T	532	56	2SE
Dang Chu	Cooper et al. (2013)	FB07		Chekha	paragneiss	27.50500	90.07800	6.60	71.8	RSCM	575	31	2SE
Dang Chu	Cooper et al. (2013)	FB07		Chekha	paragneiss	27.50500	90.07800	6.60	71.8	P-T	579	48	2SE
Dang Chu	Cooper et al. (2013)	FB85		Chekha	calc-silicate	27.55600	90.02800	5.75	77.6	RSCM	489	26	2SE
Dang Chu	Cooper et al. (2013)	FB132		GHlm	paragneiss	27.53700	89.99700	3.60	75.4	RSCM	557	37	2SE
Dang Chu	Cooper et al. (2013)	FB132		GHlm	paragneiss	27.53700	89.99700	3.60	75.4	P-T	536	75	2SE
Sarpang	Long et al. (2016)	39	BU10-21	GHlm	schist	26.93636	90.23422	0.80	6.5	RSCM	670	30	2SE
Sarpang	Long et al. (2016)	36A	BU14-9	GHlm	paragneiss	26.92744	90.20739	0.20	5.6	RSCM	719	27	2SE
Sarpang	Long et al. (2016)	35	BU14-8	GHlm	schist	26.92742	90.20919	0.15	5.5	RSCM	703	30	2SE
Sarpang	Long et al. (2016)	34	BU10-18	GHlm	paragneiss	26.92692	90.20897	0.15	5.5	RSCM	676	32	2SE
Sarpang	Long et al. (2016)	32	BU14-10B	Jaishidanda	schist	26.92519	90.20681	-0.05	5.4	RSCM	615	41	2SE
Sarpang	Long et al. (2016)	32	BU14-10B	Jaishidanda	schist	26.92519	90.20681	-0.05	5.4	P-T	623	25	2σ
Sarpang	Long et al. (2016)	27	BU14-10B	Jaishidanda	quartzite	26.92378	90.21072	-0.15	5.2	RSCM	629	36	2SE
Sarpang	Long et al. (2016)	26	BU14-4	Jaishidanda	quartzite	26.92247	90.21133	-0.20	5.2	P-T	621	25	2σ
Sarpang	Long et al. (2016)	24	BU14-12BA	Jaishidanda	schist	26.91817	90.20361	-0.55	5.1	RSCM	514	33	2SE
Sarpang	Long et al. (2016)	21A	BU14-14A	Jaishidanda	quartzite	26.91653	90.20367	-0.70	5.1	EBSD	455	50	±50

Sarpang	Long et al. (2016)	18A	BU14-17	Daling	quartzite	26.91231	90.20897	-1.30	4.7	EBSD	470	50	±50	
Sarpang	Long et al. (2016)	16A	BU14-19	Daling	quartzite	26.90786	90.20972	-1.70	4.6	EBSD	430	50	±50	
Sarpang	Long et al. (2016)	12A	BU14-22AA	Daling	quartzite	26.90083	90.20828	-2.20	4.5	RSCM	420	47	±5E	
Sarpang	Long et al. (2016)	12A	BU14-22AA	Daling	quartzite	26.90083	90.20828	-2.20	4.5	EBSD	510	50	±50	
Sarpang	Long et al. (2016)	11A	BU14-24BA	Daling	phyllite	26.90028	90.21081	-2.30	4.0	RSCM	428	31	±5E	
Sarpang	Long et al. (2016)	10A	BU14-24BA	Daling	quartzite	26.90028	90.21081	-2.30	4.0	EBSD	485	50	±50	
Sarpang	Long et al. (2016)	4A	BU14-32A	Manas	phyllite	26.88294	90.24214	-3.60	1.2	RSCM	353	61	±5E	
Sarpang	Long et al. (2016)	3A	BU14-35AA	Manas	quartzite	26.88189	90.26225	-3.75	1.0	RSCM	311	27	±5E	
Sarpang	Long et al. (2016)	1A	BU10-9A	Manas	phyllite	26.86922	90.26447	-4.45	0.0	RSCM	352	57	±5E	
Shemgang	Corrie et al. (2012)	23	K11B023	Maneting	phyllite	27.22619	90.61834	9.50	39.9	P-T	505	25	2σ	5.0 1.0 2σ
Shemgang	Corrie et al. (2012)	26	K11B026	Maneting	phyllite	27.22770	90.64047	9.00	38.8	P-T	525	25	2σ	6.0 2.5 2σ
Shemgang	Corrie et al. (2012)	32	K11B032	Maneting	phyllite	27.20350	90.67430	8.55	33.4	P-T	475	15	2σ	4.5 1.0 2σ
Shemgang	Corrie et al. (2012)	90	BU08-90	Maneting	phyllite	27.20494	90.71044	8.00	29.8	P-T	560	20	2σ	6.5 1.5 2σ
Shemgang	Corrie et al. (2012)	88	BU08-88	Chekha	quartzite	27.18875	90.70633	7.45	30.8	P-T	575	20	2σ	
Shemgang	Corrie et al. (2012)	87	BU08-87	Chekha	quartzite	27.17514	90.69531	7.00	29.8	P-T	600	25	2σ	
Shemgang	Corrie et al. (2012)	99	BU08-99	Chekha	quartzite	27.30569	90.60458	6.30	50.6	P-T	590	25	2σ	7.5 1.0 2σ
Shemgang	Corrie et al. (2012)	54	K11B054	Chekha	quartzite	27.13609	90.66539	5.80	29.5	P-T	520	15	2σ	7.5 1.0 2σ
Shemgang	Corrie et al. (2012)	95	BU08-95	Maneting	phyllite	27.22631	90.62683	5.40	39.6	P-T	475	25	2σ	5.0 1.0 2σ
Shemgang	Corrie et al. (2012)	22	K11B022	Maneting	phyllite	27.23316	90.61492	5.40	44.3	P-T	505	15	2σ	5.5 1.0 2σ
Shemgang	Corrie et al. (2012)	21	K11B021	Maneting	phyllite	27.23751	90.61330	5.40	45.0	P-T	520	15	2σ	6.0 0.5 2σ
Shemgang	Corrie et al. (2012)	89	BU08-89	Maneting	phyllite	27.19322	90.72422	5.40	31.9	P-T	575	15	2σ	7.5 1.0 2σ
Shemgang	Corrie et al. (2012)	20	K11B020	Chekha	quartzite	27.24979	90.60669	5.40	45.2	P-T	525	20	2σ	7.0 1.0 2σ
Shemgang	Corrie et al. (2012)	19	K11B019	Chekha	quartzite	27.27837	90.62914	5.40	45.8	P-T	550	15	2σ	7.5 1.0 2σ
Shemgang	Corrie et al. (2012)	66	BU08-66	Ghilmu	schist	27.12064	90.67347	5.40	25.2	P-T	540	15	2σ	6.5 0.5 2σ
Shemgang	Corrie et al. (2012)	65	BU08-65	Ghilmu	phyllite	27.12750	90.67603	5.35	25.7	P-T	550	20	2σ	6.5 1.5 2σ
Shemgang	Corrie et al. (2012)	101	BU08-101	Ghilmu	schist	27.33431	90.59397	5.35	54.3	P-T	615	20	2σ	9.5 1.0 2σ
Shemgang	Corrie et al. (2012)	63	BU08-63	Ghilmu	schist	27.12833	90.70406	5.30	26.3	P-T	570	15	2σ	7.5 1.0 2σ
Shemgang	Corrie et al. (2012)	52	K11B052	Ghilmu	schist	27.11665	90.67087	5.00	25.0	P-T	565	35	2σ	
Shemgang	Corrie et al. (2012)	53	BU08-53	Ghilmu	schist	27.11714	90.72031	4.55	25.6	P-T	620	20	2σ	9.0 1.0 2σ
Shemgang	Corrie et al. (2012)	102	BU08-102	Ghilmu	schist	27.34883	90.57372	4.55	55.7	P-T	605	20	2σ	9.0 1.0 2σ
Shemgang	Corrie et al. (2012)	109	BU08-109	Ghilmu	schist	27.44928	90.47497	4.45	66.7	P-T	675	25	2σ	9.0 1.0 2σ
Shemgang	Corrie et al. (2012)	54	BU08-54	Ghilmu	paragneiss	27.12083	90.73686	4.20	27.5	P-T	640	30	2σ	
Shemgang	Corrie et al. (2012)	106	BU08-106	Ghilmu	schist	27.41278	90.53422	4.00	63.7	P-T	615	15	2σ	9.0 0.5 2σ
Shemgang	Corrie et al. (2012)	104	BU08-104	Ghilmu	quartzite	27.38400	90.51411	3.80	59.5	P-T	580	20	2σ	9.0 0.5 2σ
Shemgang	Corrie et al. (2012)	78	BU08-78	Ghilmu	paragneiss	27.04964	90.63500	2.70	18.7	P-T	565	20	2σ	7.5 1.0 2σ
Shemgang	Corrie et al. (2012)	111	BU08-111	Ghlo	schist	27.48911	90.51094	2.65	70.5	P-T	665	15	2σ	9.5 1.0 2σ
Shemgang	Corrie et al. (2012)	58	BU08-58	Ghlo	orthogneiss	27.09250	90.76658	2.35	24.5	P-T	665	20	2σ	9.0 1.0 2σ
Shemgang	Corrie et al. (2012)	77	BU08-77	Ghilmu	paragneiss	27.03694	90.62714	1.85	16.3	P-T	595	25	2σ	7.5 1.0 2σ
Shemgang	Corrie et al. (2012)	59	BU08-59	Ghlo	paragneiss	27.08494	90.77514	1.80	23.7	P-T	670	15	2σ	10.0 0.5 2σ
Shemgang	Corrie et al. (2012)	76	BU08-76	Ghlo	paragneiss	27.01447	90.61519	1.40	15.6	P-T	665	25	2σ	10.0 1.5 2σ
Shemgang	Corrie et al. (2012)	75	BU08-75	Ghlo	schist	27.01053	90.58108	1.40	15.0	P-T	675	15	2σ	9.5 1.0 2σ
Shemgang	Corrie et al. (2012)	74	BU08-74	Ghilmu	schist	26.97725	90.55325	0.25	10.8	P-T	725	20	2σ	10.5 1.0 2σ
Shemgang	Corrie et al. (2012)	48	BU08-48	Ghilmu	schist	27.04939	90.78850	0.25	18.9	P-T	655	15	2σ	11.0 0.5 2σ
Shemgang	Corrie et al. (2012)	47	BU08-47	Ghilmu	schist	27.04936	90.79172	0.20	18.7	P-T	660	20	2σ	
Shemgang	Cooper et al. (2013)	BT1138		Maneting	phyllite	27.23400	90.61500	9.45	44.3	RSCM	566	23	±5E	
Shemgang	Cooper et al. (2013)	BT1136		Maneting	phyllite	27.22800	90.63800	9.00	38.8	RSCM	561	24	±5E	
Shemgang	Cooper et al. (2013)	BT1134		Maneting	phyllite	27.22600	90.68100	8.25	38.0	RSCM	571	25	±5E	

¹ Abbreviations for data type: RSCM = Raman spectroscopy of carbonaceous material; EBSD = electron back-scatter diffraction; P-T = conventional thermobarometry

Discussion S6: Estimation of structural height of mapped positions of the STD

The range in structural height of published mapped positions of the STD is compiled on Figures 5 and 12 in the text; the methodology for estimation of these heights is discussed here.

On the Shemgang transect, the mapped locations of the STD from Grujic et al. (2011) and Greenwood et al. (2016) were projected onto the Mangde Chu cross-section of Long et al. (2011b). At the southern end of the transect, Greenwood et al. (2016) mapped the STD at a height of 1.8 km above the MCT, and Grujic et al. (2011) at 5.4 km. At the northern end of the transect, Greenwood et al. (2016) mapped the STD at 4.4 km, and Grujic et al. (2011) at 5.4 km.

On the western side of the Dang Chu transect, the mapped locations of the STD from Greenwood et al. (2016), Grujic et al. (2011), and Long et al. (2011d) were projected onto their equivalent positions on the cross-section (Fig. 4) and tectonostratigraphic column (Fig. 5) of this study, and correspond to structural heights of 4.6 km, 4.8 km, and 6.7 km above the MCT, respectively (note: see discussion S5 above for details on estimation of the structural level of the MCT on the Dang Chu transect). For the STD as mapped by Cooper et al. (2013), the height was estimated by interpolation between the calculated heights of samples FB132 and FB85, and yielded a height of 7.5 km above the MCT.

On the east side of the Dang Chu exposure, the heights of the STD as mapped by Grujic et al. (2011), Long et al. (2011b) and Greenwood et al. (2016) were calculated based on projection of the STD relative to the basal Chekha Formation contact as mapped on Figure 3 in this study, and yielded heights of 6.7 km, 6.5 km, and 6.8 km above the MCT, respectively. The height of the STD as mapped by Cooper et al. (2013) was calculated from interpolation between the heights of samples FB20 and FB28, and yielded a height of 7.8 km above the MCT.

Discussion S7: Compilation of published strain data, and calculation of transport-parallel lengthening and transport-normal shortening.

Table S7 shows a compilation of strain data from central Bhutan. Structural heights relative to the MCT were estimated in a similar manner to the P-T samples. Samples from the Shemgang transect were projected onto the Mangde Chu cross-section of Long et al. (2011b),

samples from the Sarpang transect were projected onto the Sarpang cross-section of Long et al. (2016), and samples from the Dang Chu transect were measured off of the tectonostratigraphic column from this study (Fig. 5). Similar to the P-T samples, 5.7 km was added to sample heights relative to the base of the Chekha Formation for the Dang Chu samples, in order to estimate their height above the MCT.

The range in W_m values from the $Rs-\theta'$ method listed for each sample in Table S7 was calculated from the ± 1 standard error on θ' values listed in data tables in Long et al. (2011c), Long et al. (2016), and this study.

Restoration of the 3D strain ellipsoid for each sample to a sphere allowed estimation of elongations in the X and Y directions, and shortening in the Z direction. The Y elongation obtained from this technique was used to calculate the corrected flow-plane parallel and flow-plane normal elongations discussed below.

For calculation of flow plane-parallel (i.e., transport-parallel) lengthening and flow-plane-normal (i.e. transport-normal) shortening, the equations of Figure 10 of Law (2010), which integrate strain ratio in the X/Z direction ($Rs_{[X/Z]}$) with mean kinematic vorticity number (W_m), were utilized. Because a range of W_m values are estimated with the $Rs-\theta'$ method, due to assignment of a 1 standard error range for estimation of θ' values (e.g., Long et al., 2016; this study), the low and high ranges of W_m values were used to estimate a permissible range of lengthening and shortening values. As these values do not account for lengthening in the Y direction, they are listed in Table S7 as ‘uncorrected’.

Next, using the Y lengthening values estimated for each sample from ellipsoid restoration to a sphere (the percent stretch in Y on the graphs of Law, 2010, his Fig. 11, and Xypolias et al., 2010, their Fig. 11), corrected values for transport-parallel lengthening and transport-normal shortening were calculated that account for lengthening in Y. These corrected values were calculated for the low and high ranges of W_m for each sample. These corrected ranges are plotted on Figure 12C-D in this study, with the dot representing the middle value, and the error bars representing the lower and upper limits of estimated lengthening and shortening.

For five of the strain samples (63, 75, 95, 108, 128), only two-dimensional strain data in the X/Z plane were available. Therefore, because these samples could not be corrected for stretching in the Y direction, the transport-parallel lengthening values reported for these five

samples in Table S7 should be interpreted as maxima, and the corresponding transport-normal shortening values should be interpreted as minima.

In addition, three low-strain magnitude ($R_s \leq 1.8$) samples (68, 100, 105) yielded positive transport-parallel lengthening values between 0.5-1.5% and negative transport-normal shortening values between 5-6% (i.e., low-magnitude lengthening normal to the transport direction). Data from these three samples are plotted on Figures 12C-D, although only the positive portion of the error range for transport-normal shortening is visible on Figure 12D.

Finally, eleven low-strain magnitude (R_s typically ≤ 1.7) samples from the Shemgang transect (67, 71, 82, 83, 88, 90, 91, 94, 95, 98, and 101) exhibited high θ' values (ranging between ~ 20 - 80° , and therefore high (~ 0.70 - 1.00) corresponding W_m values. Using the equation of Law (2010), these samples yielded negative values for both transport-parallel lengthening and transport-normal shortening (most on the order of $\sim 10\%$). Therefore, these data were not able to be plotted on the Law (2010) and Xypolias et al. (2010) figures for correction of lengthening in Y , and are thus not plotted on Figures 12C-D.

Table S7 (following three pages): Compilation of strain, transport-parallel lengthening, and transport-normal shortening data from central Bhutan.

transect	data source	published sample number	original sample number	map unit	lithology	latitude (dd.ddd)	longitude (dd.ddd)	structural height relative to		low W _m from		high W _m from			
								MCT (km)	R _s [x/z]	θ' [x/z]	R _s [y/z]	θ' [y/z]	R _s [x/y]	R _s -θ'	R _s -θ'
Shemgang	Long et al. (2011c)	63	BU08-72	Jaishidanda	quartzite	26.96631	90.55781	-0.35	3.2	1	-	-	0.00	0.15	
Shemgang	Long et al. (2011c)	64	BU08-73	Manas	quartzite	26.95356	90.55161	-2.75	1.8	4	1.7	-1	1.1	0.00	0.45
Shemgang	Long et al. (2011c)	65	BU08-70	Manas	phyllite	26.95467	90.53058	-3.05	2.2	11	1.7	21	1.3	0.50	0.60
Shemgang	Long et al. (2011c)	66	BU08-71	Manas	quartzite	26.94822	90.54275	-3.40	1.8	-7	1.7	-10	1.1	0.30	0.55
Shemgang	Long et al. (2011c)	67	BU08-69A	Manas	quartzite	26.94117	90.51731	-4.15	1.9	19	1.7	-12	1.1	0.70	0.80
Shemgang	Long et al. (2011c)	68	BU08-68	Manas	phyllite	26.92622	90.50478	-5.55	1.7	-16	1.7	5	1.0	0.55	0.70
Shemgang	Long et al. (2011c)	69	BU08-110	GHlmu	schist	27.46367	90.50097	4.40	7.0	-9	3.2	4	2.2	0.75	0.80
Shemgang	Long et al. (2011c)	70	BU08-108	GHlmu	schist	27.41619	90.49331	4.25	4.0	0	2.6	-1	1.5	0.00	0.05
Shemgang	Long et al. (2011c)	71	BU08-107	GHlmu	quartzite	27.41461	90.50883	4.05	1.6	20	1.5	-12	1.1	0.65	0.80
Shemgang	Long et al. (2011c)	72	BU08-106	GHlmu	schist	27.41278	90.53422	4.00	2.8	-1	2.3	-10	1.2	0.10	0.20
Shemgang	Long et al. (2011c)	73	BU08-105	GHlmu	quartzite	27.39489	90.53150	4.75	2.4	3	2.0	-8	1.2	0.10	0.30
Shemgang	Long et al. (2011c)	74	BU08-104	GHlmu	quartzite	27.38400	90.51411	4.90	3.8	-1	2.2	-1	1.7	0.00	0.15
Shemgang	Long et al. (2011c)	75	BU08-103	GHlmu	quartzite	27.36603	90.54006	4.10	4.0	3	-	-	-	0.20	0.30
Shemgang	Long et al. (2011c)	76	BU08-102	GHlmu	schist	27.34883	90.57372	4.20	8.5	-1	3.7	3	2.3	0.05	0.15
Shemgang	Long et al. (2011c)	77	BU08-101	GHlmu	schist	27.33431	90.59397	5.35	3.5	1	2.2	-7	1.6	0.00	0.15
Shemgang	Long et al. (2011c)	78	BU08-100	Chekha	quartzite	27.32528	90.59294	8.35	3.4	-1	2.8	11	1.2	0.00	0.15
Shemgang	Long et al. (2011c)	79	BU08-99	Chekha	quartzite	27.30569	90.60458	6.30	4.1	2	1.9	-6	2.2	0.00	0.15
Shemgang	Long et al. (2011c)	80	BU08-98	Chekha	quartzite	27.27817	90.62914	6.10	1.5	-6	1.5	0	1.0	0.15	0.35
Shemgang	Long et al. (2011c)	81	BU08-97	Chekha	quartzite	27.26008	90.60025	6.30	1.5	-9	1.3	-26	1.2	0.20	0.50
Shemgang	Long et al. (2011c)	82	BU08-96	Maneting	phyllite	27.23847	90.61353	8.45	1.6	58	1.4	-31	1.1	0.80	0.95
Shemgang	Long et al. (2011c)	83	BU08-95	Maneting	phyllite	27.22631	90.62683	8.40	2.1	-81	1.4	15	1.5	1.00	1.00
Shemgang	Long et al. (2011c)	84	BU08-94	Maneting	phyllite	27.23581	90.68114	8.25	3.0	0	2.2	0	1.4	0.00	0.10
Shemgang	Long et al. (2011c)	85	BU08-93	Maneting	phyllite	27.20875	90.67039	7.80	3.0	0	2.9	1	1.0	0.00	0.20
Shemgang	Long et al. (2011c)	86	BU08-90	Maneting	phyllite	27.20494	90.71044	7.80	2.8	-5	1.6	-20	1.8	0.25	0.35
Shemgang	Long et al. (2011c)	87	BU08-89	Maneting	phyllite	27.19322	90.72422	7.70	3.0	-6	2.4	-7	1.3	0.25	0.45
Shemgang	Long et al. (2011c)	88	BU08-88	Chekha	quartzite	27.18875	90.70633	7.50	1.5	24	1.4	-7	1.1	0.75	0.85
Shemgang	Long et al. (2011c)	89	BU08-91	Chekha	quartzite	27.17578	90.69833	7.20	1.7	-10	1.6	7	1.1	0.30	0.55
Shemgang	Long et al. (2011c)	90	BU08-87	Chekha	quartzite	27.17514	90.69531	7.15	1.6	-22	1.5	-14	1.1	0.70	0.80
Shemgang	Long et al. (2011c)	91	BU08-86	Chekha	quartzite	27.16092	90.69958	6.90	1.5	37	1.5	-23	1.0	0.90	1.00
Shemgang	Long et al. (2011c)	92	BU08-49A	Chekha	quartzite	27.14817	90.69133	6.15	1.6	7	1.4	-15	1.1	0.20	0.40
Shemgang	Long et al. (2011c)	93	BU08-67	Chekha	quartzite	27.12439	90.66808	5.45	1.8	-5	1.7	1	1.1	0.00	0.15
Shemgang	Long et al. (2011c)	94	BU08-64	Chekha	quartzite	27.13264	90.68092	5.40	1.6	12	1.1	-58	1.5	1.00	1.00
Shemgang	Long et al. (2011c)	95	BU08-65	GHlmu	phyllite	27.12750	90.67603	5.30	2.5	-17	-	-	-	0.70	0.80
Shemgang	Long et al. (2011c)	96	BU08-66	GHlmu	schist	27.12064	90.67347	5.30	2.3	-12	1.6	-12	1.4	0.50	0.65
Shemgang	Long et al. (2011c)	97	BU08-85	GHlmu	schist	27.11503	90.64817	5.25	1.8	5	1.7	3	1.1	0.05	0.25
Shemgang	Long et al. (2011c)	98	BU08-84	GHlmu	quartzite	27.11083	90.65803	5.20	1.2	-70	1.2	-48	1.0	1.00	1.00
Shemgang	Long et al. (2011c)	99	BU08-83	GHlmu	quartzite	27.08908	90.64250	4.15	2.0	-3	1.7	2	1.2	0.00	0.20
Shemgang	Long et al. (2011c)	100	BU08-81	GHlmu	schist	27.06389	90.63392	3.10	1.8	15	1.7	-11	1.1	0.60	0.70
Shemgang	Long et al. (2011c)	101	BU08-80	GHlmu	quartzite	27.05728	90.63356	3.00	1.6	21	1.5	1	1.1	0.70	0.80
Shemgang	Long et al. (2011c)	102	BU08-79	GHlmu	quartzite	27.05200	90.63397	2.80	2.1	0	1.7	-3	1.2	0.00	0.10
Shemgang	Long et al. (2011c)	103	BU08-78	GHlmu	paragneiss	27.04964	90.63500	2.75	3.1	-4	1.9	8	1.6	0.20	0.30
Shemgang	Long et al. (2011c)	104	BU08-51	Chekha	quartzite	27.13739	90.70467	5.45	1.4	12	1.4	32	1.0	0.30	0.60
Shemgang	Long et al. (2011c)	105	BU08-50	Chekha	quartzite	27.13625	90.69350	5.50	1.6	-14	1.4	11	1.1	0.50	0.70
Shemgang	Long et al. (2011c)	106	BU08-63	GHlmu	schist	27.12833	90.70406	4.75	6.3	-4	1.9	4	3.3	0.30	0.50
Shemgang	Long et al. (2011c)	107	BU08-52	GHlmu	schist	27.12453	90.70847	4.15	6.9	-7	2.2	7	3.1	0.70	0.75
Shemgang	Long et al. (2011c)	108	BU08-62	GHlmu	schist	27.11722	90.71136	3.50	4.6	0	-	-	-	0.00	0.05
Shemgang	Long et al. (2011c)	109	BU08-55	GHlmu	schist	27.11633	90.73708	1.95	6.2	2	3.8	-8	1.6	0.10	0.20
Sarpang	Long et al. (2016)	19	BU14-16	Daling	schist	26.91436	90.20775	-1.05	4.2	-3	2.5	7	1.7	0.20	0.30
Sarpang	Long et al. (2016)	12	BU14-22A	Daling	quartzite	26.90083	90.20828	-2.20	3.3	2	2.5	0	1.3	0.10	0.20
Sarpang	Long et al. (2016)	11	BU14-24B	Daling	phyllite	26.90028	90.21081	-2.30	2.5	-2	1.9	2	1.3	0.05	0.20
Sarpang	Long et al. (2016)	9	BU14-23B	Manas	quartzite	26.91539	90.21214	-2.45	2.1	5	1.9	-1	1.1	0.20	0.40
Sarpang	Long et al. (2016)	7	BU14-25A	Manas	quartzite	26.89886	90.21428	-2.55	1.9	-10	1.9	-3	1.0	0.40	0.55
Sarpang	Long et al. (2016)	6	BU14-29	Manas	quartzite	26.89294	90.22986	-3.10	1.7	-5	1.6	15	1.1	0.15	0.35
Sarpang	Long et al. (2016)	5	BU10-10	Manas	phyllite	26.88669	90.26917	-3.40	1.8	-1	1.2	7	1.5	0.05	0.20
Sarpang	Long et al. (2016)	4	BU14-32	Manas	phyllite	26.88294	90.24214	-3.60	1.8	-4	1.8	0	1.0	0.10	0.30
Sarpang	Long et al. (2016)	3	BU14-35A	Manas	quartzite	26.88189	90.26225	-3.75	1.7	-3	1.5	6	1.1	0.00	0.25
Sarpang	Long et al. (2016)	2	BU14-34	Manas	phyllite	26.87681	90.25431	-3.95	1.8	-3	1.5	0	1.2	0.05	0.30
Sarpang	Long et al. (2016)	1	BU10-9	Manas	phyllite	26.86922	90.26447	-4.45	1.5	-2	1.5	-3	1.0	0.00	0.30
Dang Chu	this study	74	BU14-74	Maneting	phyllite	27.64314	90.20075	10.65	2.5	-3	1.6	8	1.6	0.15	0.25
Dang Chu	this study	125A	BU13-125A	Deshichilling	phyllite	27.61111	90.19183	9.70	2.9	2	2.7	-2	1.1	0.10	0.25
Dang Chu	this study	124	BU13-124	Deshichilling	phyllite	27.59558	90.18669	8.70	2.8	-5	2.4	2	1.2	0.25	0.35
Dang Chu	this study	123B	BU13-123B	Deshichilling	phyllite	27.58058	90.19064	8.10	2.5	-5	2.2	-5	1.1	0.25	0.35
Dang Chu	this study	120A	BU13-120A	Chekha	quartzite	27.53983	90.16672	7.35	2.1	2	1.6	-11	1.3	0.00	0.30
Dang Chu	this study	113A	BU13-113A	Chekha	phyllite	27.50733	90.08442	6.95	2.8	-3	2.6	-3	1.1	0.15	0.25
Dang Chu	this study	118B	BU13-118B	Chekha	quartzite	27.54747	90.13567	6.95	2.0	1	1.8	5	1.1	0.00	0.20
Dang Chu	this study	121	BU13-121	Chekha	limestone	27.56708	90.17622	6.90	2.3	-5	1.7	-4	1.4	0.20	0.40
Dang Chu	this study	128	BU13-128	Chekha	phyllite	27.50450	90.07872	6.60	2.5	-2	-	-	-	0.00	0.25
Dang Chu	this study	129	BU13-129	Chekha	phyllite	27.49969	90.07014	6.50	3.5	-9	3.1	-4	1.1	0.50	0.65
Dang Chu	this study	114	BU13-114	Chekha	phyllite	27.51236	90.09447	6.40	3.2	2	3.0	-2	1.1	0.10	0.25
Dang Chu	this study	131B	BU13-131B	Chekha	schist	27.49942	90.05850	5.75	2.8	-2	2.6	1	1.1	0.10	0.20

Elongation values from restoration to a sphere:				uncorrected	uncorrected	uncorrected	uncorrected	corrected	uncorrected	uncorrected
undeformed	lineation-	lineation-	foliation-	transport-	transport-	transport-	transport-	transport-	transport-	transport-
sphere	parallel (X)	normal (Y)	normal (Z)	normal	normal	normal	normal	parallel	normal	normal
diameter	lengthening	lengthening	shortening	stretch	shortening (%)	stretch	lengthening (%)	lengthening (%)	stretch	shortening (%)
	(%)	(%)	(%)	(low Wm)	(low Wm)	(low Wm)	(low Wm)	(low Wm)	(high Wm)	(high Wm)
1.79	79	0	44	0.56	44	1.79	79	79	0.57	43
1.45	24	17	31	0.75	25	1.34	34	15	0.86	14
1.55	42	10	36	0.82	18	1.22	22	12	0.91	9
1.45	24	17	31	0.79	21	1.26	26	12	0.94	6
1.48	29	15	32	1.11	-11	0.90	-10		1.37	-37
1.42	19	19	30	0.96	4	1.04	4	2	1.16	-16
2.82	148	14	65	0.76	24	1.32	32	14	0.88	12
2.18	83	19	54	0.50	50	2.00	100	69	0.50	50
1.34	20	12	25	1.10	-10	0.91	-9		1.45	-45
1.86	50	24	46	0.60	40	1.66	66	35	0.62	38
1.69	42	19	41	0.65	35	1.54	54	30	0.69	31
2.03	87	8	51	0.51	49	1.95	95	81	0.52	48
2.00	100	0	50	0.52	48	1.94	94	94	0.54	46
3.16	169	17	68	0.34	66	2.91	191	145	0.35	65
1.97	77	11	49	0.53	47	1.87	87	68	0.54	46
2.12	60	32	53	0.54	46	1.84	84	43	0.55	45
1.98	107	-4	50	0.49	51	2.02	102	117	0.50	50
1.31	14	14	24	0.83	17	1.21	21	10	0.88	12
1.25	20	4	20	0.84	16	1.20	20	15	0.97	3
1.31	22	7	24	1.45	-45	0.69	-31		2.97	-197
1.43	47	-2	30	21.99	-2099	0.05	-95		21.99	-2099
1.88	60	17	47	0.58	42	1.73	73	49	0.58	42
2.06	46	41	51	0.58	42	1.73	73	31	0.60	40
1.65	70	-3	39	0.63	37	1.60	60	66	0.66	34
1.93	55	24	48	0.61	39	1.65	65	33	0.68	32
1.28	17	9	22	1.32	-32	0.76	-24		1.71	-71
1.40	22	15	28	0.81	19	1.23	23	11	0.96	4
1.34	20	12	25	1.18	-18	0.85	-15		1.45	-45
1.31	14	14	24	2.10	-110	0.48	-52		22.16	-2116
1.31	22	7	24	0.81	19	1.23	23	16	0.88	12
1.45	24	17	31	0.75	25	1.34	34	15	0.76	24
1.21	33	-9	17	22.13	-2113	0.05	-95		22.13	-2113
1.58	58	0	37	1.00	0	1.00	0		1.26	-26
1.54	49	4	35	0.80	20	1.25	25	20	0.96	4
1.45	24	17	31	0.75	25	1.34	34	15	0.78	22
1.13	6	6	11	22.28	-2128	0.04	-96		22.28	-2128
1.50	33	13	33	0.71	29	1.41	41	25	0.73	27
1.45	24	17	31	0.99	1	1.01	1	1	1.13	-13
1.34	20	12	25	1.18	-18	0.85	-15		1.45	-45
1.53	37	11	35	0.69	31	1.45	45	32	0.69	31
1.81	72	5	45	0.59	41	1.71	71	62	0.61	39
1.25	12	12	20	0.89	11	1.12	12	5	1.09	-9
1.31	22	7	24	0.94	6	1.06	6	3	1.18	-18
2.29	175	-17	56	0.43	57	2.31	131	177	0.51	49
2.48	179	-11	60	0.67	33	1.49	49	72	0.76	24
2.14	114	0	53	0.47	53	2.14	114	114	0.47	53
2.87	116	33	65	0.41	59	2.47	147	86	0.42	58
2.19	92	14	54	0.50	50	1.98	98	75	0.53	47
2.02	63	24	51	0.55	45	1.80	80	48	0.57	43
1.68	49	13	41	0.63	37	1.58	58	41	0.65	35
1.59	32	20	37	0.71	29	1.41	41	19	0.78	22
1.53	24	24	35	0.81	19	1.23	23	11	0.91	9
1.40	22	15	28	0.78	22	1.29	29	13	0.83	17
1.29	39	-7	23	0.75	25	1.34	34	46	0.77	23
1.48	22	22	32	0.75	25	1.33	33	15	0.79	21
1.37	24	10	27	0.77	23	1.30	30	18	0.80	20
1.39	29	8	28	0.75	25	1.34	34	23	0.79	21
1.31	14	14	24	0.82	18	1.22	22	10	0.86	14
1.59	57	1	37	0.64	36	1.56	56	55	0.66	34
1.99	46	36	50	0.59	41	1.69	69	30	0.62	38
1.89	48	27	47	0.63	37	1.60	60	26	0.66	34
1.77	42	25	43	0.66	34	1.51	51	23	0.69	31
1.50	40	7	33	0.69	31	1.45	45	36	0.74	26
1.94	44	34	48	0.61	39	1.65	65	28	0.63	37
1.53	30	17	35	0.71	29	1.41	41	21	0.73	27
1.58	46	8	37	0.68	32	1.47	47	36	0.74	26
1.58	58	0	37	0.63	37	1.58	58	58	0.66	34
2.21	58	40	55	0.67	33	1.50	50	22	0.81	19
2.13	51	41	53	0.56	44	1.78	78	34	0.59	41
1.94	44	34	48	0.60	40	1.66	66	29	0.62	38

uncorrected transport- parallel stretch (high Wm)	uncorrected transport- parallel lengthening (%) (high Wm)	corrected transport- parallel lengthening (%) (high Wm)	corrected transport- parallel lengthening (%) (middle of range)	corrected transport- parallel lengthening (%) (error range)	corrected transport- normal shortening (%) (middle of range)	corrected transport- normal shortening (%) (error range)
1.76	76	76	77.5	1.5	43.6	0.5
1.16	16	8	11.5	3.5	19.7	5.8
1.10	10	4	8.0	4.0	13.6	4.5
1.07	7	2	7.0	5.0	13.6	7.2
0.73	-27					
0.86	-14	0	1.0	1.0	-5.8	9.9
1.13	13	5	9.5	4.5	18.1	6.3
2.00	100	68	68.5	0.5	49.9	0.1
0.69	-31					
1.62	62	33	34.0	1.0	39.1	0.7
1.45	45	23	26.5	3.5	33.0	2.0
1.91	91	80	80.5	0.5	48.2	0.5
1.86	86	86	90.0	4.0	47.2	1.1
2.86	186	141	143.0	2.0	65.3	0.3
1.84	84	67	67.5	0.5	46.1	0.5
1.81	81	40	41.5	1.5	45.3	0.5
1.99	99	111	114.0	3.0	50.2	0.5
1.13	13	5	7.5	2.5	14.5	2.8
1.03	3	2	8.5	6.5	9.7	6.6
0.34	-66					
0.05	-95					
1.72	72	48	48.5	0.5	42.0	0.2
1.68	68	30	30.5	0.5	41.4	0.9
1.52	52	60	63.0	3.0	35.8	1.5
1.47	47	22	27.5	5.5	35.6	3.8
0.59	-41					
1.04	4	2	6.5	4.5	11.4	7.2
0.69	-31					
0.05	-95					
1.14	14	6	11.0	5.0	15.5	3.4
1.32	32	14	14.5	0.5	24.9	0.5
0.05	-95					
0.79	-21					
1.05	5	2	11.0	9.0	12.1	7.6
1.29	29	12	13.5	1.5	23.8	1.5
0.04	-96					
1.38	38	22	23.5	1.5	28.3	1.0
0.88	-12	0	0.5	0.5	-6.0	7.3
0.69	-31					
1.44	44	30	31.0	1.0	30.8	0.2
1.64	64	58	60.0	2.0	40.2	1.2
0.92	-8	0	2.5	2.5	0.7	10.0
0.85	-15	0	1.5	1.5	-6.2	12.1
1.97	97	139	158.0	19.0	53.0	3.8
1.32	32	51	61.5	10.5	28.4	4.4
2.14	114	113	113.5	0.5	53.3	0.0
2.40	140	82	84.0	2.0	58.9	0.5
1.90	90	68	71.5	3.5	48.5	1.1
1.76	76	45	46.5	1.5	43.9	0.7
1.54	54	37	39.0	2.0	35.8	0.9
1.29	29	13	16.0	3.0	25.7	3.3
1.09	9	4	7.5	3.5	13.6	5.1
1.20	20	10	11.5	1.5	19.5	2.7
1.31	31	42	44.0	2.0	24.4	0.9
1.26	26	13	14.0	1.0	22.9	2.1
1.25	25	14	16.0	2.0	21.7	1.6
1.26	26	18	20.5	2.5	23.1	2.3
1.16	16	6	8.0	2.0	16.0	2.4
1.51	51	52	53.5	1.5	34.8	1.0
1.62	62	28	29.0	1.0	39.6	1.2
1.52	52	23	24.5	1.5	35.8	1.5
1.44	44	21	22.0	1.0	32.2	1.6
1.36	36	28	32.0	4.0	28.7	2.3
1.60	60	26	27.0	1.0	38.3	0.9
1.38	38	18	19.5	1.5	28.3	1.0
1.34	34	27	31.5	4.5	28.9	3.3
1.51	51	51	54.5	3.5	35.3	1.5
1.24	24	11	16.5	5.5	26.3	7.1
1.70	70	31	32.5	1.5	42.5	1.2
1.62	62	27	28.0	1.0	39.1	0.7

Discussion S8: Compilation of shear-sense data, and estimation of structural height relative to the MCT.

Table S8 shows a compilation of new and published shear-sense indicators observed within outcrops and thin sections from central Bhutan. These data are plotted on Figure 12F in a frequency histogram of total top-to-south and top-to-north shear-sense indicators observed versus structural height relative to the MCT. Structural heights were estimated in a similar manner to the P-T and strain samples. Localities from the Shemgang transect from Long and McQuarrie (2010) were projected onto the Mangde Chu cross-section of Long et al. (2011b), localities from the Sarpang transect were projected onto the Sarpang cross-section of Long et al. (2016), and localities from the Dang Chu transect were measured off of the tectonostratigraphic column from this study. Similar to the P-T samples, 5.7 km was added to heights relative to the base of the Chekha Formation for the Dang Chu localities, in order to approximate their height above the MCT.

Table S8 (following two pages): Compilation of data source, location, map unit, type, and shear direction information for outcrop- and thin section-scale shear-sense indicators observed in central Bhutan.

transect	data source	published stop number	original thin section number	published thin section number	latitude (dd, dddd)	longitude (dd, dddd)	height relative to MCT (km)	map unit	lithology	shear-sense indicator type	observed in:	shear-sense
Dang Chu	this study	103			27.48494	89.90569	0.45	Ghimi	paragneiss	asymmetric fold	outcrop	top-to-southeast
Dang Chu	this study	107			27.50575	89.96292	2.65	Ghlo	orthogneiss	C-type shear bands, feldspar α -clasts	outcrop	top-to-northeast
Dang Chu	this study	108			27.50481	89.98214	2.95	Ghlo	paragneiss	o-objects (leucosomes)	outcrop	top-to-south
Dang Chu	this study	108			27.50481	89.98214	2.95	Ghlo	paragneiss	o-objects (leucosomes)	outcrop	top-to-north
Dang Chu	this study	109			27.50333	90.00622	3.55	Ghlo	orthogneiss	C-type shear band	outcrop	top-to-southeast
Dang Chu	this study	109			27.50333	90.00622	3.55	Ghlo	orthogneiss	C-type shear band	outcrop	top-to-northeast
Dang Chu	this study	111			27.49856	90.03136	4.60	Ghmu	paragneiss	o-objects (leucosomes), C-type shear band	outcrop	top-to-southeast
Dang Chu	this study	112			27.49847	90.03178	4.70	Ghmu	paragneiss	o-objects (leucosomes)	outcrop	top-to-south
Dang Chu	this study	131	BU13-131B	131B	27.49772	90.05614	4.70	Ghmu	paragneiss	o-objects (leucosomes)	outcrop	top-to-south
Dang Chu	this study	136	BU13-116A, C	116A, C	27.49942	90.05850	5.75	Chekha	schist	SC fabric	thin section	top-to-south
Dang Chu	this study	166			27.54264	90.11036	5.85	Chekha	quartzite	SC fabric	thin section	top-to-north
Dang Chu	this study	290	BU13-130B	130B	27.52111	90.09767	6.15	Chekha	schist	asymmetrically-sheared boudinage	outcrop	top-to-north
Dang Chu	this study	130	BU13-130B	130B	27.50311	90.06475	6.40	Chekha	phyllite	C-type shear bands	thin section	top-to-south
Dang Chu	this study	114	BU13-114	114	27.51236	90.09447	6.40	Chekha	phyllite	asymmetric folds, rotated garnet porphyroblasts	thin section	top-to-north
Dang Chu	this study	118	BU13-118A	118A	27.54644	90.13494	6.85	Chekha	marble	asymmetric fold	outcrop	top-to-north
Dang Chu	this study	120	BU13-120B	120B	27.54747	90.13567	6.95	Chekha	phyllitic quartzite	rotated biotite porphyroblast	thin section	top-to-north
Dang Chu	this study	120			27.53983	90.16672	7.15	Chekha	phyllitic quartzite	SC fabric	thin section	top-to-north
Dang Chu	this study	120			27.53983	90.16672	7.15	Chekha	marble	asymmetric fold	outcrop	top-to-north
Dang Chu	this study	81			27.54450	90.17144	7.20	Chekha	marble	asymmetrically-sheared boudinage	outcrop	top-to-south
Dang Chu	this study	79	BU14-79A	79A	27.58814	90.18742	8.45	Deshchilling	phyllitic quartzite	SC fabric	thin section	top-to-north
Dang Chu	this study	125	BU13-125A	125A	27.61111	90.19183	9.70	Deshchilling	phyllite	SC fabric, asymmetrically-sheared boudinage	thin section	top-to-north
Dang Chu	this study	126			27.62661	90.19764	10.40	Deshchilling	quartzite	asymmetrically-sheared boudinage	outcrop	top-to-southeast
Dang Chu	this study	126			27.62661	90.19764	10.40	Deshchilling	quartzite	asymmetrically-sheared boudinage	outcrop	top-to-south
Dang Chu	this study	74			27.64314	90.20075	10.65	Maneting	phyllite	SC fabric	thin section	top-to-north
Dang Chu	this study	74	BU14-74A	74A	27.64314	90.20075	10.65	Maneting	phyllite	rotated hercynite porphyroblasts	thin section	top-to-north
Sarpang	Long et al. (2016)	37			26.93789	90.22458	0.75	Ghimi	schist	feldspar α -clast	outcrop	top-to-south
Sarpang	Long et al. (2016)	31			26.93011	90.22136	0.40	Ghimi	orthogneiss	feldspar α -clasts	outcrop	top-to-south
Sarpang	Long et al. (2016)	29	BU14-10A	31A	26.92519	90.20661	-0.05	Jashidanda	quartzite	asymmetric quartz c axis fabric	pole plot	top-to-south
Sarpang	Long et al. (2016)	29			26.92542	90.20944	-0.10	Jashidanda	schist	SC fabric, asymmetric folds	outcrop	top-to-south
Sarpang	Long et al. (2016)	29	BU14-6A	29A	26.92542	90.20944	-0.10	Jashidanda	quartzite	asymmetric quartz c axis fabric	pole plot	top-to-south
Sarpang	Long et al. (2016)	25	BU14-11A	25	26.92081	90.20568	-0.40	Jashidanda	schist	C-type shear bands, mica fish	thin section	top-to-south
Sarpang	Long et al. (2016)	24	BU14-128A	24	26.91817	90.20361	-0.55	Jashidanda	schist	rotated garnet	thin section	top-to-south
Sarpang	Long et al. (2016)	23	BU14-12A	23A	26.91817	90.20361	-0.55	Jashidanda	quartzite	asymmetric quartz c axis fabric	pole plot	top-to-south
Sarpang	Long et al. (2016)	22	BU14-148A	22	26.91653	90.20367	-0.70	Jashidanda	schist	C-type shear bands, mica fish	thin section	top-to-north
Sarpang	Long et al. (2016)	21	BU14-14A	21A	26.91653	90.20367	-0.70	Jashidanda	quartzite	asymmetric quartz c axis fabric	pole plot	top-to-south
Sarpang	Long et al. (2016)	18	BU14-17	18A	26.91231	90.20897	-1.30	Daling	quartzite	asymmetric quartz c axis fabric	pole plot	top-to-south
Sarpang	Long et al. (2016)	17	BU14-18A	17	26.91033	90.20750	-1.50	Daling	schist	C-type shear band	thin section	top-to-south
Sarpang	Long et al. (2016)	15			26.90622	90.20661	-1.95	Daling	phyllite	SC fabric	outcrop	top-to-south
Sarpang	Long et al. (2016)	12	BU14-224A	12A	26.90083	90.20828	-2.20	Daling	quartzite	asymmetric quartz c axis fabric	pole plot	top-to-north
Sarpang	Long et al. (2016)	11	BU14-248A	11A	26.90028	90.21081	-2.30	Daling	quartzite	quartz α -clast	thin section	top-to-north
Sarpang	Long et al. (2016)	8	BU14-23A	8	26.91539	90.21214	-2.45	Manas	phyllite	C-type shear band	thin section	top-to-south
Sarpang	Long et al. (2016)	5A	BU10-10A	5A	26.88669	90.26917	-3.40	Manas	phyllite	SC fabric	thin section	top-to-south
Sarpang	Long et al. (2016)	1	BU10-9A	1A	26.86922	90.26447	-4.45	Manas	phyllite	SC fabric	thin section	top-to-south
Shemgang	Long and McQuarrie (2010)	467	BU08-48		27.04939	90.78850	0.25	Ghlo	schist	mica fish	thin section	top-to-south
Shemgang	Long and McQuarrie (2010)	473	BU08-54		27.12083	90.78666	4.20	Ghmu	paragneiss	asymmetric fold	thin section	top-to-north
Shemgang	Long and McQuarrie (2010)	471	BU08-52		27.12453	90.70847	5.20	Ghmu	schist	rotated garnet porphyroblast	thin section	top-to-north
Shemgang	Long and McQuarrie (2010)	470			27.13739	90.70467	5.40	Chekha	schist	SC fabric	outcrop	top-to-south
Shemgang	Long and McQuarrie (2010)	507	BU08-75		27.01053	90.58108	1.40	Ghlo	schist	C-type shear band	thin section	top-to-south
Shemgang	Long and McQuarrie (2010)	509			27.01953	90.61506	1.50	Ghlo	orthogneiss	feldspar α -clasts	outcrop	top-to-south
Shemgang	Long and McQuarrie (2010)	510			27.02833	90.62714	1.75	Ghlo	orthogneiss	feldspar α -clasts	outcrop	top-to-south
Shemgang	Long and McQuarrie (2010)	511	BU08-77		27.03694	90.63500	1.85	Ghmu	paragneiss	rotated garnet porphyroblast	thin section	top-to-north
Shemgang	Long and McQuarrie (2010)	512	BU08-78		27.04964	90.63500	2.70	Ghmu	paragneiss	rotated biotite porphyroblast	thin section	top-to-north
Shemgang	Long and McQuarrie (2010)	513			27.05200	90.63397	2.80	Ghmu	quartzite	SC fabric	outcrop	top-to-south
Shemgang	Long and McQuarrie (2010)	515			27.06389	90.63392	3.10	Ghmu	schist	SC fabric	outcrop	top-to-south
Shemgang	Long and McQuarrie (2010)	517			27.08303	90.64319	3.90	Ghmu	schist	asymmetric folds	outcrop	top-to-south

Shengang	Long and McQuarrie (2010)	517	27.08303	90.64319	3.90	GHlmu	schist	asymmetric fold	outcrop	top-to-north
Shengang	Long and McQuarrie (2010)	519	27.11083	90.65803	5.20	GHlmu	quartzite	SC fabric	thin section	top-to-north
Shengang	Long and McQuarrie (2010)	520	27.11503	90.64817	5.25	GHlmu	schist	rotated biotite porphyroblast	thin section	top-to-north
Shengang	Long and McQuarrie (2010)	520	27.11503	90.64817	5.25	GHlmu	schist	asymmetric fold	outcrop	top-to-south
Shengang	Long and McQuarrie (2010)	486	27.12064	90.67347	5.30	GHlmu	schist	rotated biotite porphyroblast	thin section	top-to-north
Shengang	Long and McQuarrie (2010)	521	27.12817	90.66094	5.50	Chekha	schist	asymmetric folds, SC fabric	outcrop	top-to-south
Shengang	Long and McQuarrie (2010)	524	27.16092	90.69958	6.90	Chekha	quartzite	SC fabric, multiple places	outcrop	top-to-south
Shengang	Long and McQuarrie (2010)	524	27.16092	90.69958	6.90	Chekha	quartzite	SC fabric	outcrop	top-to-south
Shengang	Long and McQuarrie (2010)	531	27.19347	90.69450	7.50	Chekha	quartzite	SC fabric	outcrop	top-to-south
Shengang	Long and McQuarrie (2010)	527	27.19322	90.72422	7.70	Maneting	phyllite	asymmetric folds	thin section	top-to-north
Shengang	Long and McQuarrie (2010)	528	27.20494	90.71044	7.80	Maneting	phyllite	rotated garnet porphyroblast	thin section	top-to-north
Shengang	Long and McQuarrie (2010)	534	27.20875	90.67039	7.80	Maneting	phyllite	rotated biotite porphyroblast	thin section	top-to-north
Shengang	Long and McQuarrie (2010)	136	27.48911	90.51094	2.65	GHlo	paragneiss	rotated biotite porphyroblast	outcrop	top-to-south
Shengang	Long and McQuarrie (2010)	136	27.48911	90.51094	2.65	GHlo	paragneiss	o-object (leucosome)	thin section	top-to-south
Shengang	Long and McQuarrie (2010)	139	27.47158	90.49061	3.90	GHlo	orthogneiss	feldspar o-clasts	thin section	top-to-south
Shengang	Long and McQuarrie (2010)	140	27.46367	90.50097	4.40	GHlmu	schist	asymmetric folds	outcrop	top-to-south
Shengang	Long and McQuarrie (2010)	542	27.44928	90.47497	4.45	GHlmu	schist	rotated garnet porphyroblasts	thin section	top-to-south
Shengang	Long and McQuarrie (2010)	541	27.41278	90.53422	4.00	GHlmu	schist	SC fabric	outcrop	top-to-south
Shengang	Long and McQuarrie (2010)	540	27.36603	90.54006	4.10	GHlmu	schist	asymmetric folds	outcrop	top-to-south
Shengang	Long and McQuarrie (2010)	150	27.37158	90.52664	4.40	GHlmu	quartzite	SC fabric	outcrop	top-to-south
Shengang	Long and McQuarrie (2010)	150	27.37158	90.52664	4.40	GHlmu	quartzite	asymmetric folds	outcrop	top-to-south
Shengang	Long and McQuarrie (2010)	148	27.37783	90.52844	4.90	GHlmu	schist	SC fabric	outcrop	top-to-south
Shengang	Long and McQuarrie (2010)	147	27.39489	90.53150	4.75	GHlmu	schist	SC fabric	outcrop	top-to-south
Shengang	Long and McQuarrie (2010)	146	27.41461	90.50883	4.05	GHlmu	quartzite	outcrop-scale duplex	outcrop	top-to-south
Shengang	Long and McQuarrie (2010)	154	27.33431	90.59397	5.35	GHlmu	schist	asymmetric folds	thin section	top-to-south
Shengang	Long and McQuarrie (2010)	158	27.30569	90.60458	6.30	Chekha	quartzite	rotated garnet porphyroblasts	thin section	top-to-south
Shengang	Long and McQuarrie (2010)		27.51767	90.25553	7.20	Chekha	schist	SC fabric	outcrop	top-to-north
Shengang	Long and McQuarrie (2010)		27.51108	90.28967	6.90	Chekha	schist	asymmetric folds	outcrop	top-to-north

References cited

- Beyssac, O., Goffe, B., Petitet, J.P., Froigneux, E., Moreau, M., and Rouzaud, J.N., 2003, On the characterization of disordered and heterogeneous carbonaceous materials by Raman spectroscopy: *Spectrochimica Acta Part A*, v. 59, p. 2267–2276, doi: 10.1016/S1386-1425(03)00070-2.
- Bhattacharyya, K., Mitra, G., and Kwon, S., 2015, Geometry and kinematics of the Darjeeling–Sikkim Himalaya, India: Implications for the evolution of the Himalayan fold-thrust belt: *Journal of Asian Earth Sciences*, v. 113, p. 778-796, doi: 10.1016/j.jseaes.2015.09.008.
- Cooper, F.J., Hodges, K.V., and Adams, B.A., 2013, Metamorphic constraints on the character and displacement of the South Tibetan fault system, central Bhutanese Himalaya: *Lithosphere*, v. 5, p. 67–81, doi: 10.1130/L221.1.
- Corrie, S.L., Kohn, M.J., McQuarrie, N., and Long, S.P., 2012, Flattening the Bhutan Himalaya: *Earth and Planetary Science Letters*, v. 349-350, p. 67-74, doi:10.1016/j.epsl.2012.07.001.
- Dunnet, D., 1969, A technique for finite strain analysis using elliptical particles: *Tectonophysics*, v. 7, p. 117-136.
- Fossen, H., and Tikoff, B., 1993, The deformation matrix for simultaneous simple shearing, pure shearing and volume change, and its application to transpression–transtension tectonics: *Journal of Structural Geology*, v. 15, p. 413–422.
- Greenwood, L.V., Argles, T.W., Parrish, R.R., Harris, N.B.W. and Warren, C., 2016, The geology and tectonics of central Bhutan: *Journal of the Geological Society*, v. 173, p. 352-369, doi: 10.1144/jgs2015-031.
- Grujic, D., Warren, C.J., and Wooden, J.L., 2011, Rapid synconvergent exhumation of Miocene-

aged lower and orogenic crust in the eastern Himalaya: *Lithosphere*, v. 3, p. 346-366, doi:
10.1130/L154.1.

Holdaway, M.J., 2000, Application of new experimental and garnet Margules data to the garnet-
biotite geothermometer: *American Mineralogist*, v. 85, p. 881–892.

Holland, T.J.B., and Powell, R., 2011, An improved and extended internally consistent
thermodynamic dataset for phases of petrological interest, involving a new equation of state for
solids: *Journal of Metamorphic Geology*, v. 29, p. 333-383, doi: 10.1111/j.1525-
1314.2010.00923.x

Law, R.D., 2010, Moine thrust zone mylonites at the Stack of Glencoul: II - results of vorticity
analyses and their tectonic significance, in *Continental Tectonics and Mountain Building - The
Legacy of Peach and Horne*, edited by R.D. Law, R.W.H. Butler, R. Holdsworth, M.
Krabbendam, and R.A. Strachan, Geological Society of London Special Publication, v. 335, p.
579-602, doi: 10.144/SP335.24.

Lisle, R.J., 1977, Estimation of the tectonic strain ratio from the mean shape of deformed
elliptical markers: *Geologie en Mijnbouw*, v. 56, p. 140-144.

Lisle, R.J., 1979, Strain analysis using deformed pebbles: the influence of initial pebble shape:
Tectonophysics, v. 60, p. 263-277.

Long, S., and McQuarrie, N., 2010, Placing limits on channel flow: insights from the Bhutan
Himalaya: *Earth and Planetary Science Letters*, v. 290, p. 375-390,
doi:10.1016/j.epsl.2009.12.033.

Long, S., McQuarrie, N., Tobgay, T., and Grujic, D., 2011b, Geometry and crustal shortening of
the Himalayan fold-thrust belt, eastern and central Bhutan: *Geological Society of America
Bulletin*, v. 123, p. 1427-1447, doi:10.1130/B30203.1.

439 Long, S., McQuarrie, N., Tobgay, T., and Hawthorne, J., 2011c, Quantifying internal strain and
 440 deformation temperature in the eastern Himalaya: Implications for the evolution of strain in
 441 thrust sheets: *Journal of Structural Geology*, v. 32, p. 579-608, doi:10.1016/j.jsg.2010.12.011.
 442
 443 Long, S.P., McQuarrie, N., Tobgay, T., Grujic, D., and Hollister, L., 2011d, Geologic map of
 444 Bhutan: *The Journal of Maps*, v2011, p. 184-192, 1:500,000-scale, doi:10.4113/jom.2011.1159.
 445
 446 Long, S.P., and Soignard, E., 2016, Shallow-crustal metamorphism during Late Cretaceous
 447 anatexis in the Sevier hinterland plateau: peak temperature conditions from the Grant Range,
 448 eastern Nevada, U.S.A.: *Lithosphere*, v. 8, p. 150-164, doi: 10.1130/L501.1.
 449
 450 Long, S.P., Gordon, S.M., Young, J.P., and Soignard, E., 2016, Temperature and strain gradients
 451 through Lesser Himalayan rocks and across the Main Central thrust, south-central Bhutan:
 452 implications for transport-parallel stretching and inverted metamorphism: *Tectonics*, v. 35, doi:
 453 10.1002/2016TC004242.
 454
 455 Powell, R., and Holland, T.J.B., 1994, Optimal geothermometry and geobarometry: *American*
 456 *Mineralogist*, v. 79, p. 120-133.
 457
 458 Rahl, J.M., Anderson, K.M., Brandon, M.T., and Fassoulas, C., 2005, Raman spectroscopic
 459 carbonaceous material thermometry of low-grade metamorphic rocks: Calibration and
 460 application to tectonic exhumation in Crete, Greece: *Earth and Planetary Science Letters*, v. 240,
 461 p. 339–354, doi: 10.1016/j.epsl.2005.09.055.
 462
 463 Ramsay, J.G., 1967, *Folding and fracturing of rocks*: McGraw-Hill, New York, 560 p.
 464
 465 Ramsay, J.G., and Huber, M.I., 1983, *Techniques of Modern Structural Geology*, Vol. 1: Strain
 466 Analysis: Academic Press, London, 307 p.
 467
 468 Schelling, D., and Arita, K., 1991, Thrust tectonics, crustal shortening, and the structure of the
 469 far-eastern Nepal Himalaya: *Tectonics*, v. 10, p. 851–862, doi: 10.1029/91TC01011.

470

471 Tikoff, B., and Fossen, H., 1995, The limitations of three-dimensional kinematic vorticity
472 analysis: *Journal of Structural Geology*, v. 12, p. 1771–1784.

473

474 Whitney, D.L., and Evans, B.W., 2010, Abbreviations for names of rock-forming minerals:
475 *American Mineralogist*, v. 95, p. 185–187.

476

477 Xypolias, P., Spanos, D., Chatzaras, V., Kokkalas, S., and Koukouvelas, I., 2010, Vorticity of
478 flow in ductile thrust zones: examples from the Attico-Cycladic Massif (Internal Hellenides,
479 Greece): in *Continental Tectonics and Mountain Building - The Legacy of Peach and Horne*,
480 edited by R.D. Law, R.W.H. Butler, R. Holdsworth, M. Krabbendam, and R.A. Strachan,
481 *Geological Society of London Special Publication*, v. 335, p. 687-714, doi: 10.144/SP335.24.

482

483 Yonkee, A., 2005, Strain patterns within part of the Willard thrust sheet, Idaho-Wyoming-Utah
484 thrust belt: *Journal of Structural Geology*, v. 27, p. 1315-1343.